
Improved Training Strategies for Physics-Informed Neural Networks using Real Experimental Data in Aluminum Spot Welding

Jan A. Zak¹, Christian Weißenfels^{1,2}

Abstract Resistance spot welding is the dominant joining process for the body-in-white in the automotive industry, where the weld nugget diameter is the key quality metric. Its measurement requires destructive testing, limiting the potential for efficient quality control. Physics-informed neural networks were investigated as a promising tool to reconstruct internal process states from experimental data, enabling model-based and non-invasive quality assessment in aluminum spot welding. A major challenge is the integration of real-world data into the network due to competing optimization objectives. To address this, we introduce two novel training strategies. First, experimental losses for dynamic displacement and nugget diameter are progressively included using a fading-in function to prevent excessive optimization conflicts. We also implement a custom learning rate scheduler and early stopping based on a rolling window to counteract premature reduction due to increased loss magnitudes. Second, we introduce a conditional update of temperature-dependent material parameters via a look-up table, activated only after a loss threshold is reached to ensure physically meaningful temperatures. An axially symmetric two-dimensional model was selected to represent the welding process accurately while maintaining computational efficiency. To reduce computational burden, the training strategies and model components were first systematically evaluated in one dimension, enabling controlled analysis of loss design and contact models. The two-dimensional network predicts dynamic displacement and nugget growth within the experimental confidence interval, supports transferring welding stages from steel to aluminum, and demonstrates strong potential for fast, model-based quality control in industrial applications.

Keywords physics-informed neural networks · data-driven modeling · aluminum resistance spot welding · dynamic displacement · weld nugget diameter

1 Introduction

In recent years, automotive manufacturers have prioritized reducing vehicle weight (Barnes et al. 2000; Eckstein et al. 2010) due to regulatory scrutiny on carbon dioxide emissions from vehicles (EU 2019) or increasing safety requirements. Around a quarter of the vehicle’s total weight is constituted by the body-in-white (Roth et al. 2001); the stage of a car body’s frame before it has been painted and the installation of components like electrical wiring, powertrain, and trim. New construction methods, such as lightweight construction, are used to reduce weight. One competitive substitution for relatively weighty steel are aluminum alloys due to their high strength-to-weight ratio. This transition results in different materials with distinct properties, requiring the development of proper joining technologies. For example, aluminum exhibits approximately one-third the electric resistivity and three times the thermal conductivity of iron at room temperature (Gould 2012). Furthermore, the liquidus temperature is 660 degrees Celsius, in contrast to 1,500 degrees for steel.

Jan A. Zak (✉)

E-mail: jan1.zak@uni-a.de

¹University of Augsburg, Germany

²Center of Advanced Analytics and Predictive Sciences, University of Augsburg, Germany

The dominant joining technology for the body-in-white is resistance spot welding (RSW). It is an established process to join metal sheets in the automotive industry and other sectors, such as aerospace (Dobler et al. 1969). RSW joins two surfaces with heat generated by the resistance to the flow of electric current (Lienert et al. 2011). The contact between the surfaces is created by local clamping of the workpieces with two electrodes, as illustrated in Fig. 1. RSW of steel has been the focus of various studies investigating influencing factors, such as electrode force (Ao et al. 2009; Furukawa et al. 2006), surface conditions (Bowden and Williamson 1958; Gould 1987), electrical contact behavior (Wei and Wu 2012, 2014), and thermal phenomena (Greenwood et al. 1958; Hulst 1969). These investigations have primarily focused on either experimental approaches, which emphasize process parameters and material properties, or on the development of numerical models, mainly using the finite element method (FEM). Experimental investigations focused on various aspects, such as electrode cap lifetime (Boomer et al. 2003), electrode cap form (Bowers et al. 1990), or specific material combinations. Wei, S. C. Wang, et al. (1996) improved the modeling of nugget formation for steel RSW by integrating a current density model with experimental data from Gould (1987). Another study by J. Wang et al. (2015) validated a numerical model for aluminum-steel combinations using experimental measurements. Similarly, Prabitz et al. (2021) developed and parameterized a numerical model specifically for ultra-high-strength steel. These studies underscore the critical role of both experimental and numerical approaches in enhancing the understanding of RSW, particularly regarding different materials and optimizing welding parameters. The primary quality measure is the nugget diameter d_n [mm], proportional to the joint strength (ISO 2016a). The nugget diameter of steel RSW has been modeled using two-dimensional axisymmetric FEM simulations. Hou et al. (2007) used ANSYS, with results including temperature profiles, the heat-affected zone, and electrode displacement. The authors validated the results against the simulation results from Tsai et al. (1991), showing a good approximation. Eisazadeh et al. (2010) developed a model using ANSYS to predict nugget thickness development directly, validating their results against experimental data from Gould (1987). Saleem et al. (2012) used COMSOL to investigate the influence of electrode tip area on the welding process across three distinct cases, providing insights into how geometric parameters influence nugget formation Hou et al. (2007). Experimental studies have been conducted by Gedeon et al. (1986b) and Lane et al. (1987). Gedeon et al. data was collected on galvanized steel, which is welded with lower currents, a 133 ms upslope, and 266 ms of main weld. The authors conducted a series of experiments in which the welding process was halted at predetermined intervals to measure d_n .

In contrast to the extensive research on steel RSW, studies on aluminum alloys are comparatively limited, particularly in the context of large-scale production and big data. Florea et al. (2013) conducted an experimental study using a trial-and-error approach to identify optimal process parameters, primarily focusing on maximizing electrical current for welding 2.0-millimeter EN AW-6061 [Al Mg1SiCu]. C. Ji et al. (2010) investigated the dynamic displacement across varying process parameters and postulated a linear relationship between the maximum displacement and nugget diameter. J. Hu et al. (2022) utilized metrics, including the peak value of dynamic displacement, to predict weld quality. The authors used ensemble models and concluded that displacement is a good predictor. Kim et al. (2018) conducted experiments and simulations using commercial welding software to investigate the effect of welding time on a 1.2-millimeter sheet of EN AW-5052 [Al Mg2.5]. The simulation and experimental measurements indicate that the contact surface surpasses the liquidus temperature within the first 33.4 milliseconds of the main weld time.

Traditional physics-based approaches, such as the FEM, can solve complex physical problems accurately when parameters are well-defined. However, even with experimental measurements used for calibration and validation, FEM possesses limitations in its capacity to learn and incorporate experimental data. These data integration challenges can be addressed with Physics-informed neural networks (PINNs) (Karniadakis et al. 2021; Lagaris et al. 1998). They integrate partial differential equations (PDEs) into a neural network by regularizing for physical consistency. PINNs provide a mesh-free solution (Cuomo et al. 2022) and can alleviate the curse of dimensionality (Grohs et al. 2023; Poggio et al. 2017). Moreover, they can solve inverse problems, allowing for the direct inference of unknown parameters based on experimental data. PINNs enable the direct incorporation of experimental measurements into the computation of the solution function for initial boundary value problems. In contrast, FEM solvers typically require additional inverse procedures to infer unknown parameters from data. However, the use

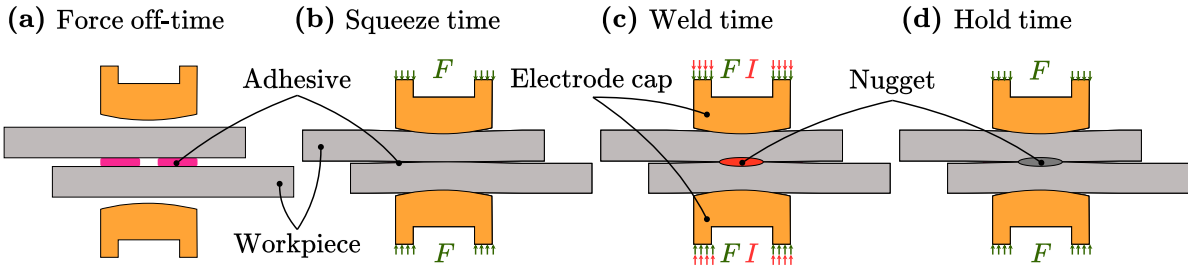


Figure 1: The RSW phases encompass the initial setup, squeezing the workpieces together, executing the weld, and holding the electrodes in place until they return to the initial setup.

of PINNs typically requires significant computational resources during training (Grossmann et al. 2023) and presents challenges in hyperparameter selection. Various scientific and engineering problems that involve PDEs have been studied, e.g., fluid mechanics (Sun et al. 2020; Wessels et al. 2020) or materials science (Y. Chen et al. 2020; Zhang et al. 2022).

Kapoor et al. (2024) utilized PINNs to solve known analytical solutions for beam bending moments, successfully identifying unknown forces. Moseley et al. (2020) solved the wave equation by augmenting the loss function with terms derived from the respective PDE. Hennigh et al. (2021) derived the geometry of a heat sink purely based on the governing PDE. Similarly, Beltran-Pulido et al. (2022) developed a two-dimensional PINN to address a magnetostatic problem, validating the results with a FEM solver. L. Wang et al. (2023) developed a PINN for two-dimensional ultrasound wave propagation, tackling the challenges of numerical solvers with discrete boundary conditions. Cai et al. (2022) provided an extensive review of three-dimensional fluid dynamics applications using PINNs and further explored the topic by conducting experiments on heat flow over an espresso cup. Their work highlighted the benefits of integrating experimental data, as they inferred velocity and pressure fields from temperature data, demonstrating how experimental inputs can enhance the training and accuracy of PINNs.

PINNs in industrial contexts remain limited, particularly in RSW. We adopt a data-driven approach and validate the predictions against experimental measurements. To this end, we divide the data into training, validation, and test sets. We develop two setups for a 1D and 2D model that integrate experimental data with governing equations to solve the temperature and displacement fields. We develop training strategies for fast loss convergence, resolving optimization challenges using experimental data, and develop a temperature-dependent material update procedure. This is a challenging task, which is achieved by delaying the activation of experimental loss and developing a rolling window for the learning rate scheduler, as well as implementing early stopping. Furthermore, we incorporate the RSW-specific welding schedule, contact heat generation, and the welding control behavior to capture the dynamic displacement curve. The resulting temperature field directly predicts the dynamic displacement and the nugget diameter, the primary quality measure.

2 Resistance Spot Welding

In industrial applications, RSW is often combined with adhesive bonding (Adams 2021). This process is generally divided into four phases (ISO 2022). The initial phase involves preparing the sheets and the application of the adhesive. During the second phase, known as squeeze time t_{st} , electrode caps contact the sheets and exert an electrode force F_{max} [kN]. In the third phase, an electric current I_{max} [kA] is applied through the electrodes following a welding schedule. This causes the material to heat up due to Joule heating, forming a weld nugget between the sheets. The final phase, hold-time t_{ht} , maintains the electrode force. The process is illustrated in Fig. 1. Heat generation primarily occurs at the faying surface between the sheets and is amplified by the adhesive. Heat at the electrode-sheet interface is managed through electrode cap cooling with T_{cool} [°C]. For steel, it is estimated that most of the generated heat is dissipated through electrode cooling and conduction into the sheets (Eagar 1990), and approximately 20% contributes to the nugget formation.

Si	Fe	Cu	Mn	Mg	Cr	Zn	Ti	Al
0.53	0.20	0.06	0.09	0.56	0.01	0.01	0.03	98.43

Table 1: Chemical composition in percentage by weight for EN AW-6014 specimen.

2.1 Experimental setup

Two EN AW-6014 with a thickness of 1.5 mm were used in our experiments. The chemical composition is listed in Tab. 1. The experimental design factors are I_{\max} and F_{\max} , and the response variable is d_n . Four forces and 22 current factor levels result in 88 factor combinations. Each combination has been welded 30 times, yielding an experimental mean and standard deviation. The welding schedule consists of a preheat current during t_{pt} of 12 kiloamperes over 400 milliseconds, a linear upslope of 70 milliseconds, and a main welding time of 90 milliseconds at I_{\max} . The welding schedule defines a current density $J = I_{\max} A_a^{-1}$, where A_a is the apparent contact area between the sheet and electrode tip, during main welding and a constant heat source with current density J_{pt} during preheating. A generic schedule can be derived:

$$J(t) = \begin{cases} J_{\text{pt}} & : 0 \leq t \leq 400 \\ J_{\text{pt}} + (J - J_{\text{pt}}) \times \frac{t-400}{470-400} & : 400 < t \leq 470 \\ J & : 470 < t \leq 560 \\ 0 & : 560 < t \leq 760 \end{cases} \quad (1)$$

The experiments have been conducted with a C-shaped transformer spot welding gun for aluminum alloys. The electric current is supplied and rectified with a medium-frequency welding transformer and controlled with a constant current control. The welding control is a Bosch Rexroth PRC7000, holding the current $I(I_{\max}, t)$ and force profile $F(F_{\max}, t)$ according to the welding schedule defined in Tab. 2. The welding schedule incorporates a preheat time t_{pt} for surface preconditioning (Luo et al. 2015) and an upslope to ensure a homogeneous temperature rise (Gedeon et al. 1986a; Lane et al. 1987). The dimensions of the upper sheet and lower sheets are 88×500 millimeters. The welds are placed in two rows from the 1st to the 15th weld spot and from the 16th to the 30th weld spot. The sheets are pretreated with a titanium-zirconium passivation and a hotmelt. A specific weld bonding BETAMATE 1640 adhesive is automatically applied beforehand. The copper-chromium-zirconium electrode caps (ISO 2016b) are of the type A0 (ISO 2009) and are cooled constantly at $T_{\text{cool}} = 19$. The cap geometry is defined in millimeters with a cap thickness of 9, cap radius of 100, and cap diameter of 20. After welding, the sheets are peeled (ISO 2015), and the average d_n is measured. The time series u was collected at a sampling rate of 1 kHz. The displacement measurement is initialized such that the position is set to zero at the start of the welding schedule, ensuring a consistent reference for subsequent displacement changes during the weld execution.

Table 2: Factor levels and controllable parameters.

Factor / Parameter	Symbol	Min./Max.		Unit	Value range
		-	+		
max. current	I_{\max}	26	47	kA	$\{I_{\max} \in \mathbb{N} 26 \leq I_{\max} \leq 47\}$
max. force	F_{\max}	5	8	kN	$\{F_{\max} \in \mathbb{N} 5 \leq F_{\max} \leq 8\}$
preheat	I_{pt}		12	kA	$\{12\}$
squeeze time	t_{st}		200	ms	$\{t_{\text{st}} \in \mathbb{Z} -200 < t_{\text{st}} \leq 0\}$
preheat time	t_{pt}		400	ms	$\{t_{\text{pt}} \in \mathbb{N} 0 < t_{\text{pt}} \leq 400\}$
upslope time	t_{ut}		70	ms	$\{t_{\text{ut}} \in \mathbb{N} 400 < t_{\text{ut}} \leq 470\}$
weld time	t_{wt}		90	ms	$\{t_{\text{wt}} \in \mathbb{N} 470 < t_{\text{wt}} \leq 560\}$
hold time	t_{ht}		200	ms	$\{t_{\text{ht}} \in \mathbb{N} 560 < t_{\text{ht}} \leq 760\}$

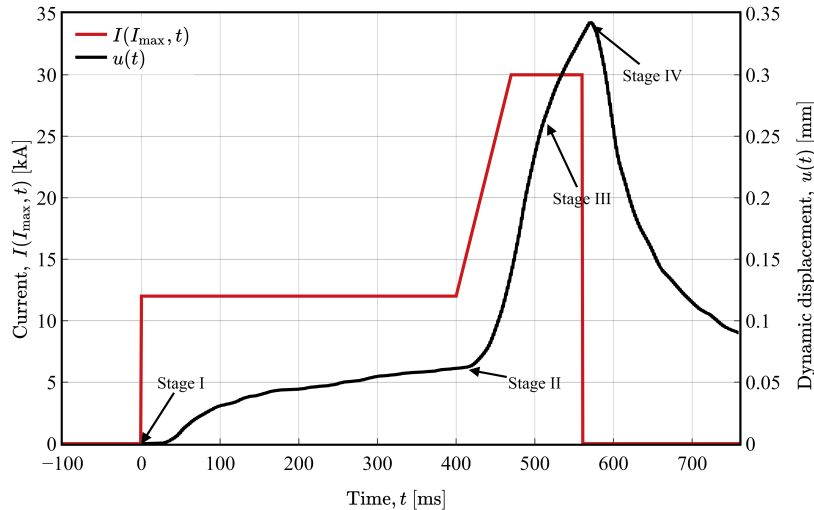


Figure 2: Welding schedule for current $I(t)$ and dynamic displacement $u(t)$. The displacement is recorded up to 760 ms.

2.2 Dynamic electrode displacement

The process parameter I_{\max} results in a welding schedule $I(I_{\max}, t)$. The force is typically held constant. An example welding schedule is illustrated in Fig. 2. An example of the measured dynamic displacement is overlaid. During welding, the sheet material thermally expands, which is measured as a dynamic displacement time series $u(t)$ [mm]. The displacement is measured in the direction of the force application with an external sensor at the welding arm and quantifies the total expansion of the sheet material. The formation of the weld nugget can be monitored through dynamic displacement measurements during the welding process. Gould (1987) developed a one-dimensional finite difference thermal model for steel. Due to the 1D model, the author investigated the development of the nugget thickness, defined as the nugget height h_n . The author mapped nugget height against welding current and time, identifying four growth stages: incubation, rapid growth, decreasing growth rate, and expulsion. While capturing the growth trends, the model overestimates nugget size in thicker sheets due to unaccounted radial heat flux. Gedeon et al. (1986b) investigated the development of nuggets and the dynamic monitoring of galvanized steel. The authors mapped stages of nugget development to u . The study identifies six displacement curve regions, with two distinct stages for the zinc coating. Without those, the displacement curve can be classified into four regions: stage I initiates with an incubation period lasting approximately the first 33 milliseconds. No visible weld nugget growth is observed, while occasional local melting occurs. However, the surface asperities flatten, which may be observed by a decrease in u . Stage II progresses with the thermal expansion of the bulk material and rapid nugget growth. The thermal expansion rate is nearly linear until the metal begins to soften or reaches the melting point. Dickinson et al. (1990) indicated a rapid growth originating from the periphery, forming an initial toroid shape that later transitions into an elliptical shape after about 50 milliseconds. During stage III, the slope of u decreases once the metal softens. The weld nugget develops, and saturation occurs. Stage IV is distinguished by a decrease or very slow growth of u . Excessive heat generation during this phase or the previous may lead to spatter, an ejection of molten material. Wei and Ho (1990) examined h_n growth in RSW of steel using an axisymmetric heat conduction model. The authors employed an enthalpy method to account for phase changes due to melting and propose an effective model for heat generation at the faying surface, validated against experimental data from Gould (1987). C. T. Ji et al. (2004) characterized the dynamic displacement and electrode force shape and investigated expulsion.

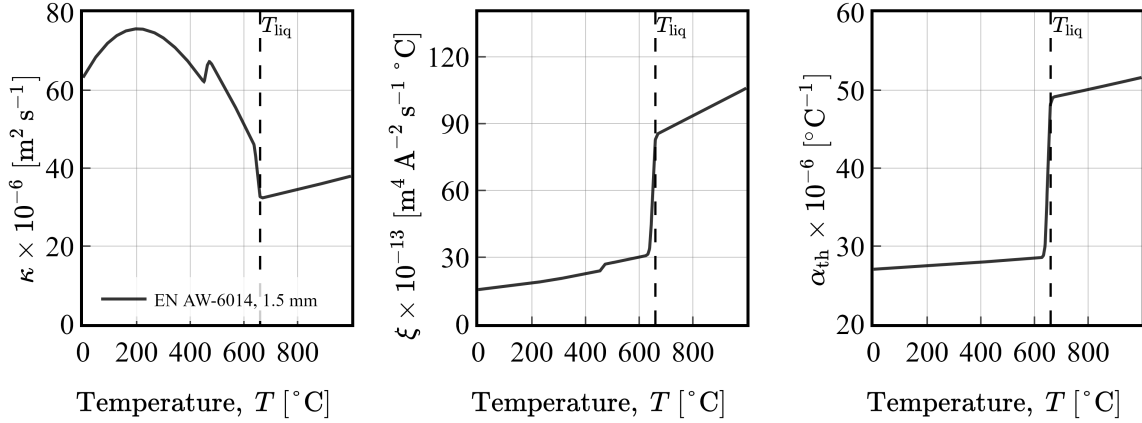


Figure 3: Experimentally measured Temperature-dependent material parameters. Thermal diffusivity κ , coefficient ξ , and thermal expansion α_{th} .

2.3 Temperature-dependent material parameters

The material parameters of EN AW-6014 have been measured for the specific electrical resistance, density, and specific heat capacity up to 550 degrees Celsius. From those quantities, the thermal diffusivity κ [$\text{m}^2 \text{s}^{-1}$], the electric resistivity per heat capacity and density ξ [$\text{m}^4 \text{K s}^{-1} \text{A}^{-2}$], and the linear thermal expansion coefficient α_{th} [K^{-1}] are defined. Values for higher temperatures and the liquidus were curve-fitted to the experimental measurements and sourced from Touloukian, Powell, et al. (1970) for thermal conductivity, Touloukian and Buyco (1971) for specific heat capacity, Mills (2002) for density, Touloukian, Kirby, et al. (1975) for thermal expansion, and Leitner et al. (2017) for electrical resistance. The phase change from the solid to the liquid phase $T_{\text{sol}} \rightarrow T_{\text{liq}}$ is modeled with the fraction of liquid material $\psi(T)$ (Kavallaris et al. 2018; Mills 2002). A piecewise function f defines the phase transition, which is generically defined as:

$$f(T, \psi) = \begin{cases} f_{\text{sol}} & : T \leq T_{\text{sol}} \\ (1 - \psi)f_{\text{sol}} + \psi f_{\text{liq}} & : T_{\text{sol}} < T < T_{\text{liq}} \\ f_{\text{liq}} & : T \geq T_{\text{liq}} \end{cases} \quad (2)$$

The resulting thermophysical material parameters are depicted in Fig. 3. Tensile tests have also been conducted up to 500 degrees, from which the hardness $H(T)$ is estimated to decrease linearly until T_{liq} .

2.4 Welding control behavior

The welding control uses an indirect measurement of the electrode force to minimize electromagnetic interference. Force is measured with a surface strain sensor on the static electrode C-shaped arm of the welding gun. It assumes linear elasticity and is calibrated against a force transducer. The sensor leverages the gun structure to measure the displacement of the arm. The result of the control is a step response $u_k(t)$ to offset the current thermal expansion $u_{\text{th}}(t)$ of the sheets. Therefore, the measured dynamic displacement does not equal the thermal expansion, $u(t) \neq u_{\text{th}}(t)$, but the following relations hold:

$$u_k(t) = u_{\text{th}}(t) \quad \rightarrow \quad u(t) = 0, \quad (3a)$$

$$u_k(t) < u_{\text{th}}(t) \quad \rightarrow \quad u(t) > 0. \quad (3b)$$

The case where $u_k > u_{\text{th}}$ is impossible because, in this case, the electrodes would no longer touch the sheet. Consequently, u equals the thermal expansion minus the control-induced adjustment:

$$u(t) = u_{\text{th}}(t) - u_k(t). \quad (4)$$

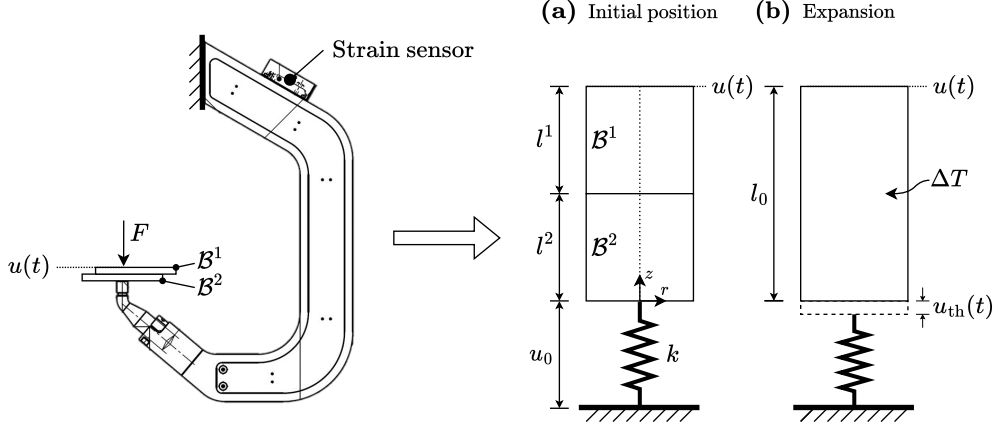


Figure 4: Simplified system model. Left: Welding gun with the application point of F and the position of the sheets. Right: Simplified two-dimensional system with a spring displacement u_k and the upper and lower sheet thicknesses l^1 and l^2 , respectively.

We estimate the step response of the welding control by assuming a proportional–integral–derivative (PID) control. The control maintains an approximately constant displacement at equilibrium; deviations from the set force value are countered by dynamically adjusting the torque T of the electric motor driving the upper electrode. This interplay is evident in Fig. 5. During the onset of the welding current, u_{th} exerts a force against the electrodes, yielding an error $e(t)$ relative to the set value. The error $e(t)$ equals the set displacement u_0 minus the actual displacement:

$$e(t) = u_0 - u(t). \quad (5)$$

Because the reference displacement u_0 is set to zero, the error equals $e = -u(t)$. A generic PID control discretized at each control time step τ can describe the response:

$$u_k(\tau) = \text{PID}(e, K_p, K_i, K_d) = K_p e(\tau) + K_i \sum_{i=0}^{\tau} e(i) \Delta t + K_d \frac{e(\tau) - e(\tau - 1)}{\Delta t}. \quad (6)$$

The previous error $e(\tau - 1)$ can be readily computed from the most recent time step, and Δt is one millisecond. The integral component can be restricted to a fixed number of previous steps to limit computation, where only the recent errors are considered in the accumulation term. We estimate the PID constants by minimizing the mean square error between the actuator, the torque $T(\tau)$, and the PID response, given the error $e(\tau) = F_0 - ku_k(\tau)$. The optimization is defined to yield the estimated proportional, integral and derivative constant:

$$\hat{K}_p, \hat{K}_i, \hat{K}_d = \arg \min_{K_p, K_i, K_d} \left\{ \text{MSE} \left(T, \text{PID} (e, K_p, K_i, K_d) \right) \right\}. \quad (7)$$

Based on this optimization, the resulting estimated PID constants for the controller are: $\hat{K}_p = 5.3 [-]$, $\hat{K}_i = 0.2 [\text{s}^{-1}]$ and $\hat{K}_d = 0.003 [\text{s}]$. Hysteresis in the force control is observable within a range of approximately 0.1%, corresponding to a tolerance band of ± 5 newton around a 5 kN setpoint. This observation is evident in Fig. 5 and manifests in the signal as values slightly below the setpoint before the onset of welding and marginally above it after the control response.

3 Methods

This chapter details the methods for modeling aluminum RSW and integrating experimental data. We begin by outlining the problem setup and the governing equations, including the key assumptions and

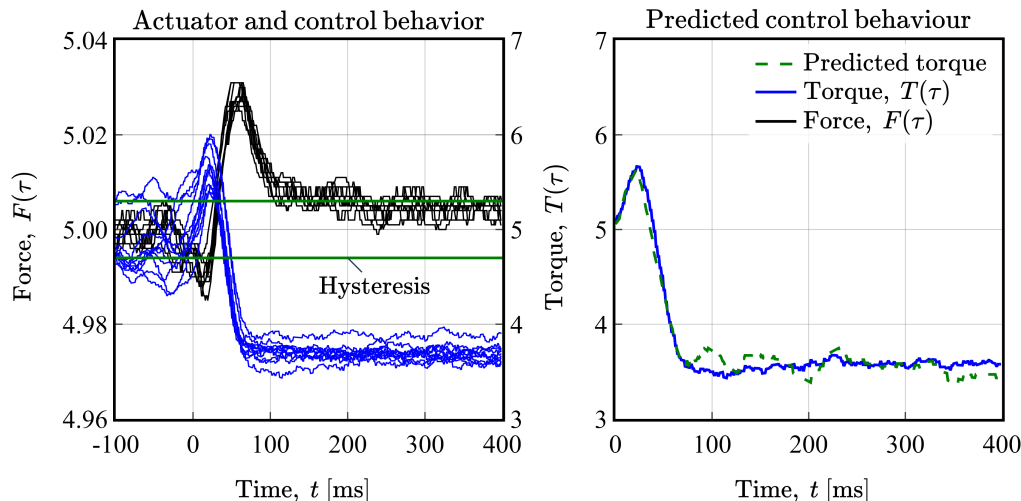


Figure 5: Left: Interplay between the control signal and the actuator. The evident hysteresis band is overlaid. Right: Estimated PID control behavior by fitting the PID constants.

simplifications made. Special attention is given to the electric contact heat generation at the faying surface. After, we review how the introduced equations and RSW-specific considerations are implemented as loss functions in a PINN. A key focus is on integrating experimental data directly into the PINN’s training. This integration is achieved through a dynamic temperature-dependent material parameter update procedure and a progressive experimental data assimilation approach that employs a sigmoid-shaped fading-in function. Furthermore, a custom rolling window scheduler and early stopping are implemented to ensure network convergence despite the introduction of new optimization objectives.

3.1 Problem setup and constitutive equations

Aluminum RSW represents a complex multiphysics problem involving coupled mechanical, thermal, and electrical fields. As an industrial welding process, the primary focus is on the temperature field because it determines the liquidus temperature and, thereby, the joining area of the metal sheets. The key characteristic of RSW is that the heat is not supplied externally but is generated internally through electrical and mechanical interactions. Magnetic and chemical effects are typically negligible in this context (Li, Lin, Lai, et al. 2009; Wei and Ho 1990), albeit electromagnetic effects have been shown to influence steel welding (Li, Lin, S. J. Hu, et al. 2007; Wei and Wu 2014). The impacts of these effects are negligible for aluminum, as discussed by Lifeng et al. (2004). To simplify the analysis and considering the computational constraints when using PINNs, we focus solely on the temperature and displacement fields, and the influence of phase-change-related latent heat is not considered because enthalpy is negligible for the transition from solid to liquid. Contact is not calculated explicitly, and sticking is assumed. To make the computational analysis feasible, we simplify the model into two models, a 1D model for the development of our methods and a two-dimensional rotationally symmetric model. Due to the high computational cost of repeated runs in 2D models, initial testing was done on 1D problems. One dimension also reduces model complexity and computational cost, which is desirable for industrial applications. The approach was then applied to an axially symmetric 2D model to represent the welding process more realistically. One dimension reduces model complexity and computational cost, which is desirable for industrial applications. However, the gold standard quality metric is the nugget diameter, which lies within the radial axis. Including the nugget diameter necessitates a transition to a 2D model.

We propose a model that simplifies the industrial machine setup, assuming a substitute model can approximate the system to a sufficient degree. This configuration and the sensor’s location are illustrated in Fig. 4. The system is modeled using a substitute in which the C-shaped welding arm is replaced by a spring. The replacement spring constant for the static electrode has been calculated based on linear

elasticity to have a stiffness of $k = 6,666 \text{ [N m}^{-1}\text{]}$. The deformation of the electrode arm is assumed to be elastic and corresponds linearly to the spring deformation, a point that is elaborated with the control equation. We also assume that there is no significant thermal expansion within the welding gun due to cooling of the electrode caps. This is because it is subjected to a limited number of welds, i.e., up to 30 welds. The substitute system also assumes that the angular momentum and body force acting on the welding gun can be neglected, as they have been calculated to have a negligible impact. Additionally, the system is considered quasi-static with a set electrode force F_{\max} and contact area A_a at the onset of electric current flow.

In our approach, the equations are the heat conduction (Lienhard et al. 2020) and the equation of linear elasticity (Landau et al. 1986). We define spatial coordinates as $\mathbf{x} = (x, y, z)$. We assume static equilibrium without body force for an isotropic, homogeneous material for temperature T and stress $\boldsymbol{\sigma}$:

$$\rho_{\text{ma}}(T)c_p(T)\frac{\partial T(\mathbf{x}, t)}{\partial t} = \nabla \cdot (\lambda_{\text{th}}(T)\nabla T(\mathbf{x}, t)) + \rho_{\text{el}}(T)J(t)^2, \quad (8)$$

$$\nabla \cdot \boldsymbol{\sigma}(\mathbf{x}, t) = 0. \quad (9)$$

Here, ρ_{ma} denotes density, c_p is the specific heat capacity, λ_{th} is the thermal conductivity, and ρ_{el} electric resistivity. Typical values are listed in Tab. 3. The constitutive relations for linear elasticity are:

$$\begin{aligned} \boldsymbol{\sigma} &= \lambda(T) (\nabla \cdot \mathbf{u}(\mathbf{x}, t) - 3\alpha_{\text{th}}(T)T(\mathbf{x}, t)) \mathbf{I} + 2\mu(T)(\boldsymbol{\epsilon} - \alpha_{\text{th}}(T)T(\mathbf{x}, t)\mathbf{I}), \\ \boldsymbol{\epsilon} &= \frac{1}{2} (\nabla \mathbf{u}(\mathbf{x}, t) + (\nabla \mathbf{u}(\mathbf{x}, t))^{\top}), \quad \lambda(T) = \frac{E_{\text{me}}(T)\nu_p}{(1 + \nu_p)((1 - 2\nu_p))}, \quad \mu(T) = \frac{E_{\text{me}}(T)}{2(1 + \nu_p)}. \end{aligned} \quad (10)$$

Here, $\mathbf{u}(\mathbf{x}, t)$ denotes displacement, $\alpha_{\text{th}}(T)$ is the coefficient of linear thermal expansion, $\lambda(T)$ and $\mu(T)$ are the first and second Lamé constants, $\boldsymbol{\epsilon}$ is the strain, $E_{\text{me}}(T)$ is Young's modulus, and ν_p is Poisson ratio. For brevity, the dependence on T and \mathbf{x} is hereafter implicit. Assuming radial symmetry, the governing equations, Eq. 8 and Eq. 9, can be formulated in cylindrical coordinates. The temperature field is therefore $T(r, z, t)$. We assume that the displacement field is totally clamped in the radial direction in our application due to the surrounding material. The assumption $u_r = 0$ is physically plausible if the system is perfectly clamped in the radial direction, yielding a dependence only on z with $u(z, t)$. The rotationally symmetric 2D form reads:

$$\rho_{\text{ma}}c_p \frac{\partial T}{\partial t} = \frac{1}{r} \frac{\partial}{\partial r} \left(\lambda_{\text{th}} r \frac{\partial T}{\partial r} \right) + \frac{\partial}{\partial z} \left(\lambda_{\text{th}} \frac{\partial T}{\partial z} \right) + \rho_{\text{el}} J^2, \quad (11)$$

$$(\lambda + 2\mu) \frac{\partial^2 u}{\partial z^2} = (3\lambda + 2\mu) \alpha_{\text{th}} \frac{\partial T}{\partial z}. \quad (12)$$

The initial condition for T is set to a reference room temperature T_{ref} and $u = 0$. The thermal boundary condition on the electrode-sheet interface is defined with a heat flux. The boundaries are visualized in Fig. 6, with $\partial \mathcal{B} = \Gamma^{\text{es}} \cup \Gamma^{\text{ss}} \cup \Gamma^{\text{s}}$. Here, Γ^{es} is the boundary towards the electrode caps, Γ^{ss} is the faying surface, and Γ^{s} is the radial boundary towards the sheet material. Using the Biot number $Bi = h_{\text{th}} \lambda_{\text{th}}^{-1}$, the axial boundary is defined:

$$\frac{\partial T}{\partial z} = Bi [T(0, t) - T_{\text{ref}}] \quad \text{on} \quad \Gamma^{\text{es}}. \quad (13)$$

The heat transfer coefficient h_{th} has been measured by Piott et al. (2020) to be $25,000 \text{ [W m}^{-2} \text{K}^{-1}\text{]}$ at a coolant flow rate of 3 liters per minute and a comparable machine setup. Cylindrical coordinates require a different approach for the radial heat flux (Lienhard et al. 2020) than the axial heat flux. As heat flows to a reference temperature, the cylindrical geometry changes, illustrated in Fig. 6c. The condition reads at $r = 1$:

$$\frac{\partial T}{\partial r} = \frac{1}{\ln L} [T_{\text{ref}} - T(r = 1)] \quad \text{on} \quad \Gamma^{\text{s}}. \quad (14)$$

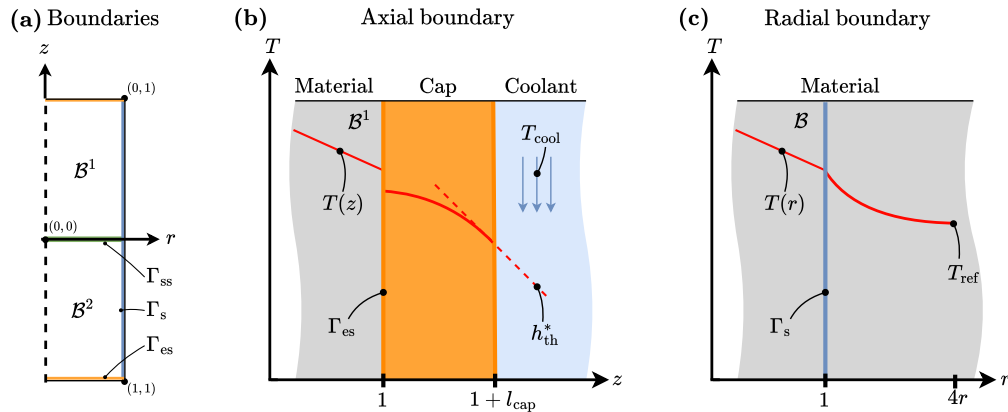


Figure 6: Left: The configuration of the upper \mathcal{B}^1 and lower sheet \mathcal{B}^2 . Middle: An illustration following Budynas et al. (2020) of the Neumann boundary condition at the upper sheet and the electrode cap, along with the effect of electrode cooling. The heat transfer coefficient h_{th}^* describes the flux between the electrode cap and the coolant. Right: An illustration of the radial boundary with a reference temperature T_{ref} .

Here, L is a chosen distance at which \bar{T}_{ref} is known. From experiments, we observed that at a distance of $L = 20$ millimeters, the temperature of the sheet material is unaffected.

3.2 Electric contact heat generation at the faying surface

Modeling the contact behaviour on a microscopic level is considered a complicated process (Eagar 1990; Wei and Ho 1990) because the initial electrical and thermal contact situation is hard to measure. Quantitatively, Kaars et al. (2016b) proposed a temperature-dependent exponentially decaying contact resistance R_c between two sheets of hot-dipped steel. An exemplary decay is shown in Fig. 7c. S. C. Wang et al. (2001) also studied the contact resistance for steel RSW and found that the initial rapid decrease of the dynamic electrical resistance is primarily due to the reduction in film resistance R_f . Two key electrical contact resistances arise in RSW: one at the electrode-sheet interface and another at the faying surface. The heat generated here is of particular interest, as the remains of the adhesive create a high contact resistance, and the region experiences the highest heat accumulation. This is because the faying surface is farthest from the cooled electrodes. In contrast, the heat generated at the cooled electrode-sheet interface is minimal. The contact resistance R_c consists of constriction R_e and film resistance R_f . The former is primarily caused by surface roughness, which constricts current streamlines at discrete contact points, and the latter by the presence of films of matter, such as oil, adhesives, or other contaminants, commonly found in industrial settings. The resistances for a local contact spot have been derived by Holm (1967) as:

$$R_e = \frac{\rho_{\text{el}}}{2a}, \quad \text{and} \quad R_f = \frac{\rho_{\text{el}}^f l_f}{a^2 \pi}, \quad (15)$$

where a is the effective radius, ρ_{el} is the electric resistivity of the material or film, and l_f is the film thickness. The effective radius is used because the apparent area A_a differs from the real area A_r (Bowden and Tabor 2001), sometimes termed the load-bearing area. The electrical resistance of a metal-to-metal contact can be assumed to consist of uniformly distributed contact spots a_i (Greenwood et al. 1958):

$$A_r = \sum_{i=1}^n a_i^2 \pi = n a^2 \pi. \quad (16)$$

Based on experimental evidence, Woo et al. (1980) demonstrated that the real contact area shows a linear dependence on the applied load, that is, F_{\max} and the Vickers hardness H :

$$n\pi a^2 = \frac{F_{\max}}{H}. \quad (17)$$

Holm and Greenwood referenced RSW as an application example, and research on it has since been conducted. For example, Crinon et al. (1998) experiment on pretreated surfaces and James et al. (1997) conduct a rudimentary FEM analysis of the contact resistance using Holm's formula. A model for R_c has been developed by S. C. Wang et al. (2001) with a multiphysics setup. The authors stress that the mechanical and electrical properties of the materials, such as hardness and resistivity, are temperature-dependent, and they applied this method in subsequent studies Wei and Wu (2012, 2014). Their definition of local contact resistance builds upon Eq. 15 and Eq. 17 and is given by:

$$R_c^A = \frac{\rho_{\text{el}}}{2} \sqrt{\frac{n\pi H}{F_{\max}}} + \rho_{\text{el}}^f \frac{nl_f H}{F_{\max}}. \quad (18)$$

Here, n is the number of contact spots, ρ_{el}^f is the electric resistivity of the film, and l_f is the film thickness. For epoxy resins, like the weld bonding adhesive, a typical value for ρ_{el}^f is between 10^6 and 10^9 ohm-meters (Mousavi et al. 2022; Tang et al. 2013). The right-hand side of Eq. 18 corresponds to the constriction and film resistance, respectively. It is commonly argued that during welding, the number of contact spots remains constant while their size increases. Directly measuring the real contact area is nearly impossible, especially in industrial settings.

Alternatively, a model can be defined with the essential relation described by Eq. 17, directly relating the contact resistance to the applied force and material hardness. Weißenfels et al. (2009) considered spreading resistance Holm (1967) based on a projection of 3D models on the surface and considering the parallel connection of the spots at the contact surface. The authors defined a pressure-dependent contact resistance for electric contact between two metals. To appropriately compare both models, we extend the constriction-based contact resistance by a film resistance term for the forward model:

$$R_c^B = \frac{1.05\rho_{\text{el}}}{4} \sqrt{\frac{\pi H}{F_{\max}}} + \rho_{\text{el}}^f \frac{l_f H}{F_{\max}}. \quad (19)$$

The faying surface Γ^{ss} is of key interest at which the weld nugget develops. We treat the thermal heat generated on Γ^{ss} as an additive heat source to the heat equation, cf. Eq. 8. Although N. Chen et al. (2019) suggested that most adhesive is squeezed out during t_{st} , Zhao et al. (2018) demonstrated an increased R_c due to the remaining adhesive. The authors investigated the effect of the adhesive using dual-phase steel and summarized that the nugget diameter is increased by higher R_c with weld bonding (Kaars et al. 2016a; Piott et al. 2019; Zhao et al. 2018). Assuming n parallel contact spots, the contact heat is defined as the sum of bulk heat generation and contact heat defined in Eq. 18 and using J defined in Eq. 2:

$$q_c^A = \rho_{\text{el}} J^2 + \frac{A_a}{l_f} \frac{R_c^A}{n} J^2, \quad \text{at} \quad z = 0.5, \quad (20)$$

$$q_c^B = \rho_{\text{el}} J^2 + \frac{A_a}{l_f} R_c^B J^2, \quad \text{at} \quad z = 0.5. \quad (21)$$

Pressure and current density must be considered radially when expanding the setup with a radial dimension. The applied local pressure is assumed to follow a Hertzian pressure distribution, a model with a well-established analytical solution, as shown in Fig. 7a. Concerning the contact heat generation, theoretical discussions by Greenwood et al. (1958) suggested that the temperature distribution relies solely on the current density J and the contact geometry. It was proposed that T follows approximately a normal distribution increasing towards the periphery of the contact area, as shown in Fig. 7b.

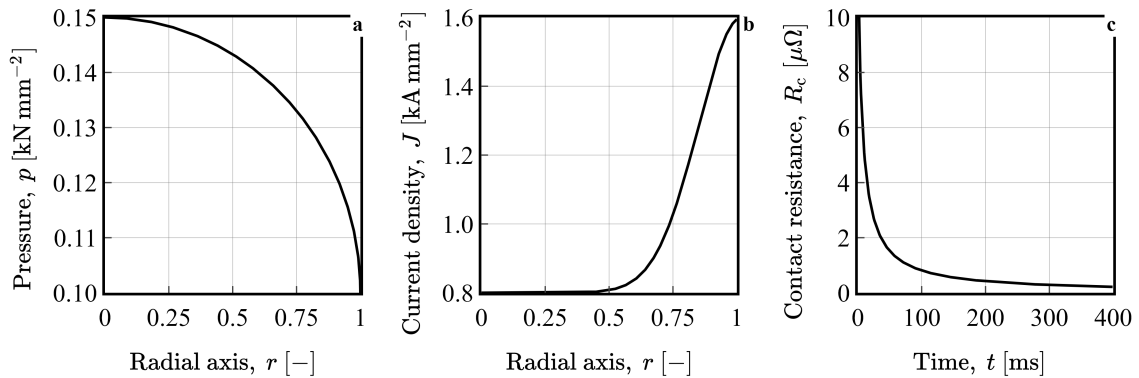


Figure 7: Hertzian contact pressure, Greenwood et al. (1958) current density, and Kaars et al. (2016a) logarithmic decay of R_c , all on Γ^{ss} .

3.3 Reformulation and non-dimensionalization

We introduce two key variables of the heat equation: thermal diffusivity κ and the ratio of ρ_{el} to ρ_{ma} and c_p , which is termed electro-thermal dissipation ξ :

$$\kappa = \frac{\lambda_{th}}{\rho_{ma}c_p}, \quad \text{and} \quad \xi = \frac{\rho_{el}}{\rho_{ma}c_p}. \quad (22)$$

Non-dimensionalization is a common method in mathematics and physics to transform a given system into a dimensionless form (Langtangen et al. 2016; S. Wang, Sankaran, et al. 2023). In the case of PINNs, it acts as normalization of the data, which is often implemented to enhance numerical optimization and convergence of gradient-based learning (Jung 2022). For this reason, non-dimensionalization is important for PINNs, among others, because it alleviates convergence issues (S. Wang, Teng, et al. 2021; S. Wang, Yu, et al. 2022). We non-dimensionalize Eq. 11 and Eq. 12 by introducing the following characteristic dimensionless variables: For clarity, in the subsequent discussion, we omit the explicit notation of the dimensionless variables:

$$\bar{r} = \frac{r}{r_c}, \quad \bar{z} = \frac{z}{z_c}, \quad \bar{t} = \frac{t}{t_c}, \quad \bar{T} = \frac{T - T_0}{T_c}, \quad \bar{u} = \frac{u}{u_c}. \quad (23)$$

Here, the variables r_c , z_c , t_c , T_c , and u_c represent the corresponding characteristic scales for the radial, axial, temporal, temperature, and displacement variables. We define a characteristic time scale to consider the primary effect in the axial direction. Defining the characteristic displacement as:

$$t_c = \frac{\rho_c c_c z_c^2}{\lambda_c}, \quad \text{and} \quad u_c = \frac{(3\lambda + 2\mu)T_c z_c \alpha_{th}}{(\lambda + 2\mu)}. \quad (24)$$

After grouping, the non-dimensionalized form reads:

$$\frac{\partial \bar{T}}{\partial \bar{t}} = \frac{z_c^2}{r_c^2} \frac{1}{\bar{r}} \frac{\partial}{\partial \bar{r}} \left(\lambda_{th} \bar{r} \frac{\partial \bar{T}}{\partial \bar{r}} \right) + \frac{\partial}{\partial \bar{z}} \left(\lambda_{th} \frac{\partial \bar{T}}{\partial \bar{z}} \right) + \frac{z_c^2}{T_c} \xi J^2, \quad (25)$$

$$\frac{\partial^2 \bar{u}_z}{\partial \bar{z}^2} = \frac{\partial \bar{T}}{\partial \bar{z}}. \quad (26)$$

3.4 Physics-informed neural network setup

A general formulation of PINNs (Raissi, Perdikaris, et al. 2017a,b) starts with a neural network (NN) f_{NN} defined with a set of internal, learnable parameters, i.e., weights and biases denoted as θ , and

Typical values	Unit	Value
c_p	$\text{J kg}^{-1} \text{K}^{-1}$	890
ρ_{ma}	kg mm^{-3}	2.7×10^{-6}
κ	$\text{mm}^2 \text{ms}^{-1}$	0.06
λ_{th}	$\text{W mm}^{-1} \text{K}^{-1}$	0.16
ρ_{el}	Ωmm	3.66×10^{-5}
l_f	mm	10^{-5}
ρ_{el}^f	Ωmm	10^5
ν_p	–	0.33
H, E_{me}	N mm^{-2}	430, 70
n	–	120,000
A_a	mm^2	79
$T_{\text{ref}}, T_{\text{liq}}, T_{\text{sol}}$	$^\circ\text{C}$	20, 660, 630

Table 3: Typical values for EN AW-6014.

Characteristic value	Unit	Value
r_c	mm	5
z_c	mm	3
t_c	ms	$\rho_c c_c z_c^2 \lambda_c^{-1}$
T_c	$^\circ\text{C}$	T_{liq}
u_c	mm	$T_c \alpha_{\text{th}} z_c$

Table 4: Characteristic values for the non-dimensionalization.

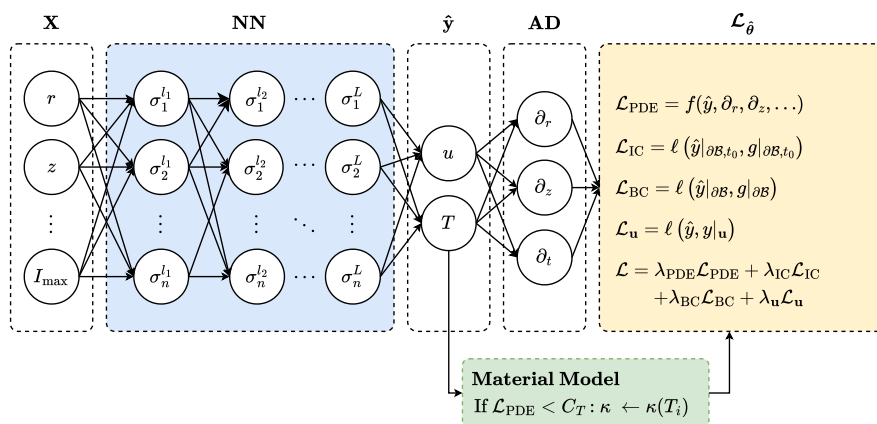


Figure 8: Illustration of the PINN setup for RSW with temperature-dependent material model and dynamic displacement.

configurations chosen before training that steer the learning process, i.e., hyperparameters λ . Within a single layer $l \in L$, the weight matrix and bias vector are referred to as $\mathbf{w}^l \in \mathbb{R}^{z_l \times z_{l-1}}$ and $\mathbf{b}^l \in \mathbb{R}^{z_l}$ (Lu 2020). with this setup, a neural network can be defined recursively with a neuron z :

$$\begin{aligned}
 \text{input layer: } & z^0(\mathbf{X}) = \mathbf{X} \in \mathbb{R}^{d_{\text{in}}}, \\
 \text{hidden layer: } & z^l(\mathbf{X}) = \sigma^l(\mathbf{w}^l z^{l-1}(\mathbf{X}) + \mathbf{b}^l) \in \mathbb{R}^{n_l}, \quad \forall l \in [1, L-1], \\
 \text{output layer: } & z^L(\mathbf{X}) = \mathbf{w}^L z^{L-1}(\mathbf{X}) + \mathbf{b}^L \in \mathbb{R}^{d_{\text{out}}}.
 \end{aligned} \tag{27}$$

The continuous-time approach uses a f_{NN} to approximate the hidden solution, parametrizing and training to learn θ , thereby approximating the PDE. The rationale behind this approach lies in utilizing the universal approximation theorem, asserting that f_{NN} can effectively approximate any function (Cuomo et al. 2022), and also coupled fields:

$$f_{\text{NN}}(r, z, t; \theta) \approx [\hat{T}(r, z, t), \hat{u}(r, z, t)]. \tag{28}$$

Fig. 8 illustrates the PINN setup, where r , z , and t represent the space and time domains. The f_{NN} is regularized with the partial differential equations for both fields, cf. Eq. 26. Incorporating a welding schedule into a PINN requires time-dependent heat generation. A realistic welding schedule introduces an upslope and hold time, as defined in Eq. 1. However, this is nontrivial due to the discontinuities in the first derivative of the welding schedule. For the temperature field, the non-dimensionalized heat

equation is set as the PDE loss, denoted as $\mathcal{L}_{\text{PDE}}^T$. The initial condition is enforced with $\mathcal{L}_{\text{IC}}^T$, where the initial temperature is referenced to room temperature, which is set to 23 degrees, $T = T' - T_{\text{room}}$. The boundary consists of axial and radial heat flux and is regularized by $\mathcal{L}_{\text{BC}}^T$. The axial heat flux, defined in Eq. 13, can be directly implemented as a boundary loss function. Because the direction of the heat flux is unknown to the automatic differentiation, the absolute value of the temperature gradient is necessary to enforce an outward flux. The radial heat flux is defined with Eq. 14:

$$\mathcal{L}_{\text{PDE}}^T = \frac{1}{|\mathcal{D}_{\text{PDE}}|} \sum_{i=1}^{|\mathcal{D}_{\text{PDE}}|} \left[\frac{\partial \hat{T}_i}{\partial t} - \frac{z_c^2}{r_c^2} \frac{1}{r} \frac{\partial}{\partial r} \left(\lambda_{\text{th}} r \frac{\partial \hat{T}_i}{\partial r} \right) - \frac{\partial}{\partial z} \left(\lambda_{\text{th}} \frac{\partial \hat{T}_i}{\partial z} \right) - Q \right]^2, \quad (29a)$$

$$\mathcal{L}_{\text{IC}}^T = \frac{1}{|\mathcal{D}_{\text{IC}}|} \sum_{i=1}^{|\mathcal{D}_{\text{IC}}|} \left[\hat{T}_i - T_{\text{ref}} \right]^2, \quad (29b)$$

$$\mathcal{L}_{\text{BC}}^T = \frac{1}{|\mathcal{D}_{\text{BC}}|} \sum_{i=1}^{|\mathcal{D}_{\text{BC}}|} \left[\underbrace{\left| \frac{\partial \hat{T}_i}{\partial z} \right| - Bi [T(r, 0, t) - T_{\text{ref}}]}_{\text{Axial flux}} \right]^2 + \left[\underbrace{\left| \frac{\partial \hat{T}_i}{\partial r} \right| - \frac{1}{\ln L} [T_{\text{ref}} - T(1, z, t)]}_{\text{Radial flux}} \right]^2. \quad (29c)$$

Here, \hat{T}_i denotes the i -th estimate, and T_{ref} has different reference values in each term. The heat source depends on the bulk material or the faying surface, as defined in Eq. 20:

$$Q = \begin{cases} \frac{z_c^2}{T_c} \xi J^2 & : r_i, z_i \in \mathcal{B} \\ \frac{z_c^2}{T_c} \frac{1}{c_p \rho_{\text{ma}}} q_c^{A/B} & : r_i, z_i \text{ on } \Gamma^{\text{ss}} \end{cases} \quad (30)$$

The number of contact spots in Eq. 18 is set as a learnable parameter for the neural network to steer contact heat generation. The available data for aluminum RSW includes the measurement of the formed nugget diameter d_n . The measurement of d_n is used to penalize the PINN to a temperature above the liquidus at $t = 560$. Afterward, the cooling period begins. At this point, the maximum temperature is reached. This information is referred to as a goal loss $\mathcal{L}_{\text{goal}}$, as defined in (Seo 2024). This penalty can be added to find a solution that not only solves the governing equations but also achieves an additional objective. In \mathcal{D}_{d_n} , points are identified where the temperature must have surpassed the liquidus value to form the molten nugget. The proposed loss formulation is based on two key considerations. First, it avoids penalizing temperatures that exceed the liquidus temperature, focusing only on the available information: the temperature is above this threshold rather than specifying an exact value. Second, it preserves the computational graph that the automatic differentiation generates. This is accomplished by applying a masking operation to \hat{T} during backpropagation and computing the temperature difference relative to T_{liq} . We define \mathcal{D}_{d_n} on Γ^{ss} and non-dimensionalize the temperature using T_c :

$$\mathcal{L}_{d_n} = \frac{1}{|\mathcal{D}_{d_n}|} \sum_{i=1}^{|\mathcal{D}_{d_n}|} \left[\min \left\{ \hat{T}(r, 0.5, t), T_{\text{liq}} \right\} - T_{\text{liq}} \right]^2. \quad (31)$$

For the displacement field, the network regularizes the governing equation with the loss $\mathcal{L}_{\text{PDE}}^u$. The initial condition is enforced to be zero with $\mathcal{L}_{\text{IC}}^u$. The radial displacement is constrained to zero $\mathcal{L}_{\text{BC}}^u$. The experimental data is added using \mathcal{L}_u at $z = 1$. It is the estimated welding control response u_k , defined in Eq. 6, minus the experimental dynamic displacement $u(t)$. The loss functions for the displacement field

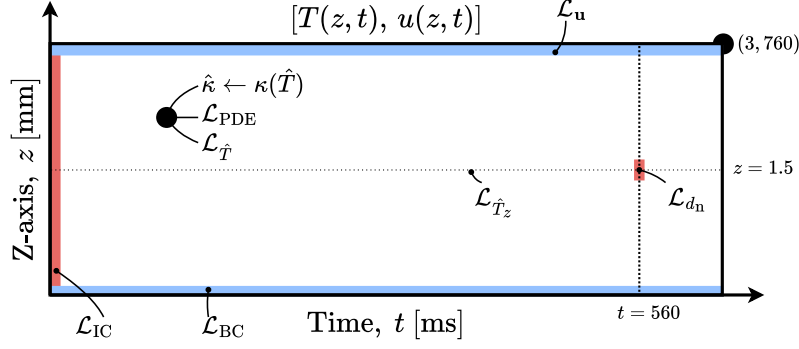


Figure 9: Illustration of the losses for RSW. Blue indicates the boundary condition and red the initial condition and \mathcal{L}_{d_n} . The goal losses \mathcal{L}_u are indicated in yellow, where the two lines are illustrative for \mathcal{D}_u and \mathcal{D}_r , respectively. The dotted line represents the location of $\mathcal{L}_{\hat{T}_z}$, while one collocation point demonstrates the application of the material update, \mathcal{L}_{PDE} and $\mathcal{L}_{\hat{T}}$. The r-axis is omitted for this illustration.

are:

$$\mathcal{L}_{\text{PDE}}^u = \frac{1}{|\mathcal{D}_{\text{PDE}}|} \sum_{i=1}^{|\mathcal{D}_{\text{PDE}}|} \left[\frac{\partial^2 \hat{u}_i}{\partial z^2} - \frac{\partial \hat{T}_i}{\partial z} \right]^2, \quad (32a)$$

$$\mathcal{L}_{\text{IC}}^u = \frac{1}{|\mathcal{D}_{\text{IC}}|} \sum_{i=1}^{|\mathcal{D}_{\text{IC}}|} \hat{u}_i(z, 0)^2, \quad (32b)$$

$$\mathcal{L}_{\text{BC}}^u = \frac{1}{|\mathcal{D}_{\text{BC}}|} \sum_{i=1}^{|\mathcal{D}_{\text{BC}}|} \hat{u}_i(0, t)^2 \quad \text{and} \quad \mathcal{L}_u = \frac{1}{|\mathcal{D}_{\text{BC}}|} \sum_{i=1}^{|\mathcal{D}_{\text{BC}}|} [\hat{u}(1, t) - u_k(t) - u(t)]^2. \quad (32c)$$

Radial symmetry may be defined at $r = 0$ as an equilibrium condition. The same condition can be defined for the z-axis at $z = 0.5$:

$$\frac{\partial T}{\partial r} = 0 \quad \text{on} \quad r = 0, \quad \text{and} \quad \frac{\partial T}{\partial z} = 0 \quad \text{on} \quad \Gamma^{\text{SS}}. \quad (33)$$

The latter condition is not as trivial as the radial equilibrium. If the material sheet thickness is unequal, the sheet-sheet interface is no longer at $z = 0.5$, and we can enforce it at another z value. The governing equation naturally constrains the first derivative, ensuring it approaches zero along the z-axis:

$$\mathcal{L}_{\hat{T}_z} = \frac{1}{|\mathcal{D}_z|} \sum_{i=1}^{\mathcal{D}_z} \hat{T}_z^2 \quad \text{and} \quad \mathcal{L}_{\hat{T}_r} = \frac{1}{|\mathcal{D}_r|} \sum_{i=1}^{\mathcal{D}_r} \hat{T}_r^2. \quad (34)$$

The complete loss is defined as:

$$\mathcal{L} = \lambda_{\text{PDE}}(\mathcal{L}_{\text{PDE}}^T + \mathcal{L}_{\text{PDE}}^u) + \lambda_{\text{IC}}(\mathcal{L}_{\text{IC}}^T + \mathcal{L}_{\text{IC}}^u) + \lambda_{\text{BC}}(\mathcal{L}_{\text{BC}}^T + \mathcal{L}_{\text{BC}}^u) + \lambda_u \mathcal{L}_u + \lambda_{d_n} \mathcal{L}_{d_n} + \mathcal{L}_{\hat{T}_z} + \mathcal{L}_{\hat{T}_r}. \quad (35)$$

Here, the hyperparameters λ weight the individual loss terms. Weighting the contribution of each individual loss term is achieved by weighting, which is crucial when terms vary in magnitude or importance. S. Wang, Teng, et al. (2021) did not define a λ_{PDE} , reasoning that the collocation point is the main objective, whereas Cuomo et al. (2022) used hyperparameters on all terms of \mathcal{L} . Fig. 9 illustrates the losses. The loss function \mathcal{L} serves as a means to enforce the adherence of the neural network to the PDE, boundary condition, and observed data. Subsequently, the optimization criterion for Eq. 35 can be expressed with $\hat{\theta}$ as the estimated parameters of the neural network: $\hat{\theta} = \arg \min_{\theta} \{\mathcal{L}\}$.

The dataset consists of domain, initial, boundary, and aggregated experimental data. The dataset is partitioned into training, validation and test sets. The collocation points of \mathcal{D}_{PDE} consist of space

and time domains and are expanded with the process parameters $\{r, z, t, I_{\max}, F_{\max}\}$. We use Latin hypercube sampling (McKay et al. 1979) to sample more representative random uniform samples than independent, identically distributed sampling (Bergstra and Bengio 2012). It has been utilized by Raissi, Yazdani, et al. (2020) to sample collocation points from each \mathcal{B} . The initial condition dataset is defined as predictor-response pairs $\mathcal{D}_{\text{IC}} := \{\mathbf{X}_{\text{IC}}, \mathbf{y}_{\text{IC}}\}$, where \mathbf{X} is the predictor and \mathbf{y} the response. The boundary conditions are evaluated on $\mathcal{D}_{\text{BC}} := \{\mathbf{X}_{\text{BC}}, \mathbf{y}_{\text{BC}}\}$ on the boundary Γ^{es} to enforce the Neumann conditions.

The experiments span 22 current and four force levels, yielding 88 combinations. For each combination, 30 repetitions are welded. Each experiment measures dynamic displacement and nugget diameter. From these repetitions, 88 mean values are calculated. We disregard the first weld spot due to electrical contact irregularities, as the electrode caps are redressed before each sheet. The target dynamic displacement is denoted as \mathbf{y}_u and the nugget diameters as \mathbf{y}_{d_n} . The dataset is structured by organizing the predictors \mathbf{X} and the responses \mathbf{y} variables according to individual welding experiments. Neither target has the same shape as \mathcal{D}_{PDE} , which is defined by its space-time domains. The targets have the shape of time for \mathbf{y}_u , and a single time step at the end of the welding time $t = 560$ for \mathbf{y}_{d_n} . During training, the displacement field can be aggregated to match the dimension of \mathbf{y}_u , and the temperature field can be evaluated on the specific points of \mathbf{y}_{d_n} . An example of both targets is:

$$\mathbf{y}_u = \begin{bmatrix} u(z = 1, t = 0) \\ u(z = 1, t = 1) \\ \dots \\ u(z = 1, t = 760) \end{bmatrix}, \quad \mathbf{y}_{d_n} = \begin{bmatrix} T(r = 0.0, z = 0.5, t = 560) \\ T(r = 0.1, z = 0.5, t = 560) \\ \dots \\ T(r = 1.0, z = 0.5, t = 560) \end{bmatrix}. \quad (36)$$

Concerning the evaluation protocol, the dataset is divided into 60% training, 20% validation, and 20% test sets based on individual welding experiments. This procedure ensures that data points from the same weld are not split across different welds, thereby preventing information leakage between welds, as the data is fully contained within each weld. The training set $\mathcal{D}^{\text{train}}$ is used to fit the model, the validation set \mathcal{D}^{val} is used for hyperparameter optimization, and the test set $\mathcal{D}^{\text{test}}$ is reserved for evaluating the final model. This method ensures the evaluation reflects the ability to generalize to unseen welds, which is an advantage compared to numerical simulation. An important consideration for PINNs is the setup of the datasets. For example, the initial condition \mathcal{D}_{IC} may be incorporated within the boundary condition with $\mathcal{D}_{\text{IC}} \in \mathcal{D}_{\text{BC}}$ (Raissi, Perdikaris, et al. 2017a). We find that explicit datasets for the initial, boundary, and domain points enable a more transparent interpretation of the loss terms and model convergence.

3.5 Training strategies for integrating experimental data

This section introduces a method for dynamically updating temperature-dependent material parameters using the network’s predicted temperature. We further discuss a delayed loss activation to mitigate training instability during early training. Subsequently, we present a progressive data assimilation approach that gradually introduces experimental goal losses. Lastly, we propose a rolling window for the learning rate scheduler and early stopping, which prevents premature convergence issues.

3.5.1 Temperature-dependent material parameter update and delayed loss activation

When temperature-dependent material parameters are available, they must not be inferred by the PINN. However, the material parameters are not always available as a continuous analytical function that is easily differentiated. An alternative is to provide the parameters as a lookup table. To incorporate the experimental values with a lookup table, the product and chain rule must be applied to separate the terms. For example, in the axial term of Eq. 29a, the chain rule is expanded to:

$$\frac{\partial}{\partial z} \left(\lambda_{\text{th}}(T(z)) \frac{\partial T}{\partial z} \right) = \frac{\partial \lambda_{\text{th}}(T(z))}{\partial T} \left(\frac{\partial T}{\partial z} \right)^2 + \lambda_{\text{th}}(T(z)) \frac{\partial^2 T}{\partial z^2}. \quad (37)$$

Automatic differentiation can solve the left-hand side of this equation, but requires $\lambda(T)$ to be a continuous function, which is not available. We use the right-hand side with the defined functions using Eq. 2

and the derivatives with respect to T using look-up tables. The material parameters can be updated using \hat{T} by matching the current values to their distinct room temperature values. Our proposed procedure dynamically updates the material parameters for each instance in a batch, $i \in b$, during each training step. This corresponds to a specific point (r, z, t) , where the PINN estimates the temperature \hat{T} . For example, $\xi(T)$ is included in the model and updated to $\hat{\xi}$ given \hat{T} for each collocation point i . We define the update procedure as:

$$\hat{\lambda}_{\text{th}}^i = \lambda_{\text{th}}(\hat{T}^i), \quad \hat{\xi}^i = \xi(\hat{T}^i), \quad \hat{\alpha}_{\text{th}}^i = \alpha_{\text{th}}(\hat{T}^i). \quad (38)$$

During the initial stages of training, the network predicts unrealistic temperatures and displacements. The network predicts all possible values, including negative temperatures, which distorts the optimization process. As material parameters are temperature-dependent, unreasonable values would be used at the very beginning of the training. For example, negative temperatures must be handled by clamping or extending the material parameter values. In our implementation, the network is initially trained to predict reasonable values for \hat{T} , after which the material properties are updated. This approach helps avoid the instability caused by unreasonable temperature estimates early in training. We delay the activation of Eq. 38. This strategy is inspired by the approach of Zhang et al. (2022) and Moseley et al. (2020), where \mathcal{L}_{PDE} is delayed. Rather than using a fixed training step for activation, we employ a threshold value for the estimated temperature, $C_{\hat{T}}$, also illustrated in Fig. 8. The material parameters are added to the optimization once the following condition is fulfilled:

$$\mathcal{L} \leq C_{\hat{T}}. \quad (39)$$

In addition, a loss function is introduced to prevent the PINN from predicting negative temperatures in general. During model development, it was observed that \hat{T} was occasionally below zero during the initial stages of training. This issue arises in the context of competing objectives within \mathcal{L}_{PDE} . To safeguard the prediction, the PINN is constrained by imposing a penalty for $\hat{T} < 0$. The loss is added to the total loss in Eq. 35, without a hyperparameter. The points are sampled from \mathcal{D}_{PDE} and preserve the automatic differentiation by masking the prediction array against negative infinity:

$$\mathcal{L}_{\hat{T}} = \frac{1}{|\mathcal{D}_{\text{PDE}}|} \sum_{i=1}^{|\mathcal{D}_{\text{PDE}}|} \left[\min \left\{ 0, \max \left\{ \hat{T}_i, -\infty \right\} \right\} \right]^2. \quad (40)$$

3.5.2 Progressive experimental data assimilation

Instead of introducing the loss terms for the experimental data abruptly, we employ a scaling factor f that gradually fades in the additional loss following a sigmoid-shaped function. The gradual introduction of additional loss terms ensures a smooth transition, resulting in minimized contribution from the added loss at the early stage. This enables the network to adapt without destabilizing gradients or hindering convergence because the network does not have to handle competing objectives. An example of an abrupt introduction is given Fig. 10. The experimental data losses, i.e., $\{\mathcal{L}_{d_n}, \mathcal{L}_u\}$, are added to the optimization when the threshold is undercut, as previously argued. The fading-in process begins when the threshold $C_{\hat{T}}$ is undercut, denoted as the reference epoch s_{ref} . The fading duration is defined with a number of transition epochs s_{trans} during which the partial loss is denoted as $\mathcal{L}'_{\text{goal}}$. Here, the scaling factor is defined with the steepness of the sigmoid curve set to 0.01:

$$\mathcal{L}'_{\text{goal}} = f \times \mathcal{L}_{\text{goal}} \quad \text{where} \quad f = \frac{1}{1 + e^{-0.01(s - s_{\text{ref}} - s_{\text{trans}})}}. \quad (41)$$

3.5.3 Rolling window learning rate scheduler and early stopping

Common types of learning rate schedulers track the performance of a metric and reduce the learning rate after a specified number of epochs with no improvement, or after a fixed step size, such as every 1,000 epochs. In performance-based approaches, a parameter known as patience is often employed to prevent overly frequent reductions in the learning rate. This is the number of epochs, N_{bad} , during

which the metric is allowed not to improve before triggering a reduction. This results in an issue when integrating experimental data because an additional goal loss increases the total loss. Ordinary learning rate schedulers often result in a rapid reduction of the learning rate, which can lead to training stalling. This refers to the situation where the learning progress severely decreases or stops completely. We define a dynamic approach that leverages a rolling window with a length k to mitigate this effect. This enables considering only losses within a rolling window from $s - k$ to s . The best loss during this rolling window is denoted as $\mathcal{L}_{\text{best}}$:

$$\mathcal{L}_{\text{best}} = \min\{\mathcal{L}_{s-k}, \dots, \mathcal{L}_s\}. \quad (42)$$

The new number of bad epochs N'_{bad} is updated based on the most recent loss metric \mathcal{L}_s as follows:

$$N'_{\text{bad}} = \begin{cases} N_{\text{bad}} + 1 & : \mathcal{L}_s > \mathcal{L}_{\text{best}} \\ 0 & : \mathcal{L}_s \leq \mathcal{L}_{\text{best}} \quad \text{or} \quad N_{\text{bad}} = k \end{cases} \quad (43)$$

The learning rate is reduced only when N_{bad} exceeds the patience:

$$\eta = \begin{cases} \eta & : N_{\text{bad}} < k \\ 0.1 \times \eta & : N_{\text{bad}} = k \end{cases} \quad (44)$$

Here, an order of magnitude is chosen for reducing η . The main advantage is that the optimizer can retain a high learning rate while optimizing for additional optimization criteria, such as experimental data. Furthermore, stalling is prevented, and the functionality of reducing η is maintained if the loss does not converge. While the rolling window strategy offers advantages, it introduces additional computational overhead due to updating the set $\min\{\mathcal{L}_{s-k}, \dots, \mathcal{L}_s\}$. However, this is worth the cost because the total training time is reduced.

The equivalent logic also applies to early stopping (Prechelt 2012), a regularization technique to prevent overfitting. In its original sense, early stopping detects plateaus or stalls in the validation loss and terminates training after a specified grace period, known as patience. The validation step in PINN training would sample domain or boundary points from the same domain as the training step. Additionally, frameworks often disable gradient backpropagation during validation because the network's weights are not updated, rendering training of PINNs highly inefficient when backpropagation is deliberately allowed. We monitor the PINN loss to detect a plateau and stop the training before the model diverges. The early stopping must also be defined using a rolling window. The increased loss from the newly added experimental losses might be interpreted as a lack of improvement, potentially triggering early stopping prematurely.

4 Results and Discussion

In this section, we begin by establishing a quantitative benchmark through training a PINN on a 1D heat equation with homogeneous Dirichlet boundaries and a sinusoidal heat source, for which an analytical solution exists. A benchmark loss value is established for the analytical solution, serving as a reference for assessing the PINN accuracy. Building upon this reference, we introduce a temperature-dependent material update procedure that utilizes a loss threshold. This section emphasizes the significance of controlled activation of material parameter updates to ensure stable and efficient training. Next, we explore hyperparameter optimization and training strategies using a 1D model. The initial focus on a one-dimensional approach is motivated by significantly lower computational costs without the overhead of large collocation grids. We demonstrate the effectiveness of the training strategies when incorporating additional experimental data constraints. We also compare inverse and forward PINN approaches for modeling contact heat generation and examine the resulting temperature fields and dynamic displacement in one dimension. After demonstrating these strategies in this controlled setting, we extend the model to a two-dimensional case, including the growth of the nugget diameters. By comparing it with the 2D variant, we discuss whether the 1D analysis is sufficient to describe aluminum RSW and thus the quality of the welding. All models used in this chapter are listed in Tab. 5, describing the achieved loss and their neural network parameters.

	Note	Section	Referenced Figures	Train Loss	Params
#1	Analytical model	4.1	-	3.01×10^{-7}	50×2
#2	Immediate \mathcal{L}_u	4.2.1	Fig. 10	3.51×10^0	66×3
#3	No smoothing	4.2.1	Fig. 10	0.11×10^0	66×3
#4	No rolling window	4.2.1	Fig. 10	1.95×10^{-2}	66×3
#5	Smoothing and rolling	4.2.1	Fig. 10	6.53×10^{-7}	66×3
#6	Forward model	4.2.2	Fig. 13	17.8×10^{-6}	66×3
#7	Inverse model	4.2.2	Fig. 13	1.30×10^{-6}	66×3
#8	1D model	4.2.3	Figs. 11,12,15,16	1.30×10^{-6}	66×3
#9	2D model	4.3	Figs. 17,18,19,20,21,22,23	6.02×10^{-6}	66×3

Table 5: Overview of trained models. Parameters describe the neural network layer size and number of layers.

4.1 Reference solution with Dirichlet boundaries and sinusoidal heat source

The magnitude of the loss can serve as an indicator of the quality of the solution. To meaningfully interpret whether a loss value is sufficient, a reference loss is needed. Without a direct analytical or numerical reference, we use a simple 1D problem with a known analytical solution as a benchmark for the magnitude of the loss. The heat equation can be simplified to a one-dimensional, non-homogeneous partial differential equation subject to homogeneous Dirichlet boundary conditions. Specifically, the temperature at the boundaries is fixed, with $T(0, t) = T(1, t) = 0$ while the initial temperature distribution is given by $T(z, 0) = 0$. The resulting formulation of the problem is (Farlow 1993):

$$\frac{\partial T(z, t)}{\partial t} = \kappa \frac{\partial^2 T(z, t)}{\partial z^2} + \sin(\pi z). \quad (45)$$

In this case, q_s is assumed to be constant within the domain $z \in [0, 1]$. We specify the heat source as $\sin(\pi z)$ to derive the analytical solution:

$$T(z, t) = e^{-(\pi\kappa)^2 t} \sin(\pi z) + \frac{1}{(\pi\kappa)^2} \left(1 - e^{-(\pi\kappa)^2 t}\right) \sin(\pi z). \quad (46)$$

We train a PINN to solve the Dirichlet setup to obtain a benchmark loss. The one-dimensional problem is defined as:

$$\mathcal{L}_{\text{PDE}} = \frac{1}{|\mathcal{D}_{\text{PDE}}|} \sum_{i=1}^{|\mathcal{D}_{\text{PDE}}|} \left[\frac{\partial \hat{T}_i}{\partial t} - \lambda_{\text{th}} \frac{\partial^2 \hat{T}_i}{\partial z^2} - \sin(\pi z) \right]^2, \quad (47)$$

$$\mathcal{L}_{\text{IC}} = \frac{1}{|\mathcal{D}_{\text{IC}}|} \sum_{i=1}^{|\mathcal{D}_{\text{IC}}|} \hat{T}_i^2, \quad \mathcal{L}_{\text{BC}} = \frac{1}{|\mathcal{D}_{\text{BC}}|} \sum_{i=1}^{|\mathcal{D}_{\text{BC}}|} \hat{T}_i^2. \quad (48)$$

The model achieves a reference loss of 3.01×10^{-7} , at which no visual difference to the analytical solution is observed.

4.2 Test of training strategies for integrating experimental data in one dimension

Since it is unknown which set of hyperparameters is optimal for our learning task, exploring a wide range of hyperparameters is usually necessary. With a number of weighting terms in Eq. 35, this exploration leads to a hyperparameter optimization problem. This optimization is a formal process (Bergstra, Bardenet, et al. 2011) of searching the hyperparameter space, in which we make as few prior assumptions as possible, thereby leaving the selection to the algorithm. Bergstra and Bengio (2012) experimentally showed that exploring the search space randomly is a favorable approach compared to manual or grid search. All continuous hyperparameters are defined on a logarithmic scale to span several orders of magnitude efficiently. We use hyperopt (Bergstra, Yamins, et al. 2013) to suggest configurations according

Hyperparameter	Value range
number of hidden layers	[2; 6]
size of hidden layers	[8; 512]
optimizer	Adam, Adadelta, RMSprop, limited-memory BFGS
layer initialization	(normal or uniform) Xavier or Kaiming
activation function	tanh, GELU, ELU
initial learning rate η	$[10^{-6}; 10^{-1}]$
number of datapoints $ \mathcal{D}_{\text{PDE}} $	$[10^3; 10^5]$
$\lambda_{\text{PDE}}, \lambda_{\text{IC}}, \lambda_{\text{BC}}, \lambda_u, \lambda_{d_n}$	$[10^{-2}; 10^1]$

Table 6: Hyperparameter search space.

to a random sampling strategy, outperforming manual and grid searches in practice (Bergstra and Bengio 2012). The neural network size is explored, ranging from two to six hidden layers, each with 8 to 512 neurons. The weighting of the terms of each loss term is searched on a scale between 10^{-2} and 10^1 . We focus on three key hyperparameters for the network: the optimizer, which governs how the network’s weights are updated during training; the activation function, which introduces non-linearity to the model; and the weight initialization method, which sets the initial values of the weights. To evaluate how different optimization dynamics affect convergence, we investigate four popular algorithms: Adam, Adadelta, RMSprop, and limited-memory Broyden–Fletcher–Goldfarb–Shanno (BFGS). The choice of the activation function is an active field of research with no conclusive consensus. Recognizing that activation functions are crucial to model stability and training, we examine tanh, GELU, and ELU. ReLU and LeakyReLU are not included because, as Sitzmann et al. (2020) noted, it breaks the second derivative. Since the initial distribution of network weights can influence gradient behavior at the start of training, we compare two widely used initialization schemes: Xavier initialization and Kaiming initialization, using both normal and uniform distributions. Furthermore, we do not use batch normalization as it has been shown to break the meaning of the derivative. The search space is summarized in Tab. 6. The hyperparameter optimization for the 1D setup used $\mathcal{D}^{\text{train}}$ and was evaluated on \mathcal{D}^{val} . This resulted in a model with three hidden layers and 66 neurons. In fact, increasing the number of neurons consistently decreased the final loss, suggesting potential overfitting. Although previous studies (Raissi, Perdikaris, et al. 2017a) have utilized the BFGS optimizer, the hyperparameter results suggest that the Adam optimizer offers smoother convergence and facilitates the implementation of training strategies. The layer initialization has little effect, with Xavier having an edge. The tanh activation function, a threshold of $C_{\hat{T}} = 0.001$, and an initial learning rate of $\eta = 10^{-3}$ were determined to be the most effective for our application. The number of data points is 10,000, and the regularization parameters were set to $\lambda_u = 0.7$ with all other parameters set to one.

4.2.1 Smoothing factor and rolling windows

As previously discussed, the abrupt introduction of additional constraints, such as time series loss, \mathcal{L}_u , frequently leads to optimization conflicts and stalling in PINN training. We investigate the effect of two key strategies: smoothing the introduction of the new loss terms and employing a rolling window for the learning rate scheduler and early stopping. Both strategies are defined in Eq. 41 and Eq. 43. This part focuses on integrating a goal loss, which is why the models are trained on a mockup goal loss with a heat source defined in Eq. 20. The mock-up goal loss is set twice as high as the default solution without goal loss. The loss is later replaced by the experimental dynamic displacement and is referred to as \mathcal{L}_u . We introduce three distinct models to evaluate the effects. The first model, which immediately activates \mathcal{L}_u , without waiting for a $C_{\hat{T}}$, illustrates the need for the threshold. The second model, which uses no smoothing, highlights the immediate spike in loss that results from the abrupt addition of a constraint. The third uses smoothing but no rolling window. The fourth model combines both strategies, where we initially trained the PINN to solve the governing equation and boundary conditions. Once $C_{\hat{T}}$ is met, the time series loss \mathcal{L}_u and material parameter update are added to the optimization. As argued before, when the additional constraints are added abruptly, the training almost always stalls immediately. This is

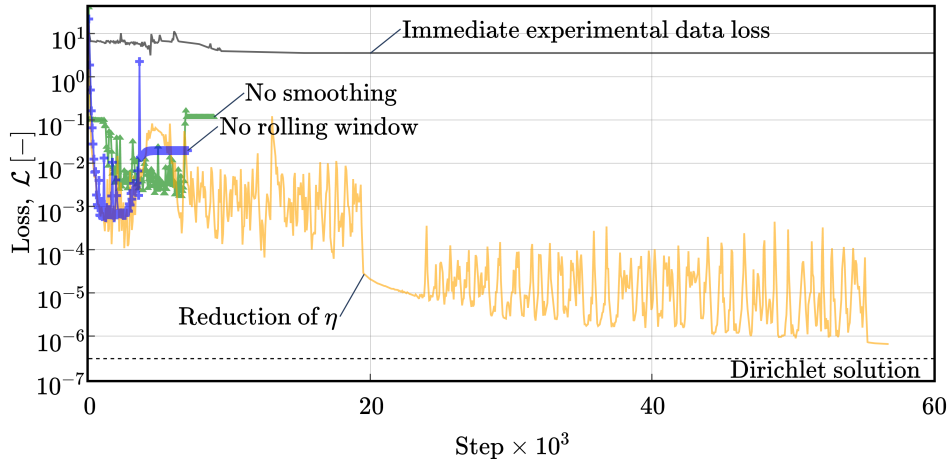


Figure 10: Effect of smoothing factor and rolling window on separate models on mockup goal losses. The exact reference epoch depends on when the threshold $C_{\hat{T}}$ is undercut. Grey: Immediate activation of the experimental goal loss, resulting in no convergence and eventually in stalling. Green: The abrupt introduction of additional optimization criteria can result in stalling. Blue: Gradual introduction results in stalling because the learning rate is reduced too fast. The training is stopped. Yellow: A rolling window allows for a relatively high learning rate while balancing the optimization criteria.

because an optimization conflict arises between the introduced data objective and the existing PDE and boundary-condition objectives. This conflict is visible with the green trace in Fig. 10, where the training stalls after adding \mathcal{L}_u . To overcome this, we gradually introduced the constraints using the smoothing function defined in Eq. 41 over 1,500 epochs. This allows a smooth, continued convergence of the other losses, e.g., \mathcal{L}_{PDE} and \mathcal{L}_{BC} . The blue trace shows the effect of the smoothing function.

A secondary issue is that the total \mathcal{L} inevitably remains above the lowest previous value for an extended time. This prematurely triggers the learning rate scheduler and early stopping. We addressed this by implementing a rolling window, cf. Eq. 43, with a window size equal to the scheduler’s patience parameter, which is optimal. In our models, the number of steps is 1,000. The strategy enables the training to begin with comparatively high learning rates, at $\eta = 10^{-3}$, while maintaining loss convergence. The rolling window only considers the last $k + 500 = 1,500$ steps. Training is terminated if no decrease in loss is observed within the entire window. The yellow trace in Fig. 10 shows a gradual increase in loss, followed by a rapid return to the previous level of loss. The network’s loss steadily decreases to values much closer to the Dirichlet benchmark. These results indicate that combining a smoothing term and a rolling window yields improved convergence behavior and lower final loss than abrupt constraint introduction.

4.2.2 Comparison of an inverse and forward PINN for contact heat generation

We train a complete 1D model on $\mathcal{D}^{\text{train}}$ and validate using the prediction on $\mathcal{D}^{\text{test}}$ and the confidence interval of the experimental data. The model learns from the real-world experimental dynamic displacement data. Training is allowed up to 10^5 epochs, but early stopping ends the training if no improvement is detected or the analytical reference loss is achieved: $\mathcal{L} \leq 3.01 \times 10^{-7}$. Loss convergence was achieved despite a spike once $C_{\hat{T}}$ was undercut, as shown in Fig. 11. In other experiments without the smoothing strategy, the spike was observed to be higher by a factor of 10^3 , resulting in immediate stalling, as evident in Fig. 10. This spike is crucial to the model’s convergence. The training strategies effectively balance the spike and yield better results, as indicated by the convergence of \mathcal{L}_{PDE} . Other loss spikes around $\mathcal{L} = 10^{-4}$ are not uncommon and align with findings from various studies, where sharp increases in loss are typically followed by rapid recovery. This behavior has been observed across a range of model architectures and applications, as noted in the works of He et al. (2023), Hennigh et al. (2021), and Zhang et al. (2022). In addition, $\mathcal{L}_{\hat{T}}$ vanishes after 34,000 epochs, and the training terminates after the last learning rate reduction. Those kinds of spikes are not attributed to a specific type of loss. The training does not achieve Dirichlet accuracy but produces continuous and reasonable temperature and displacement fields.

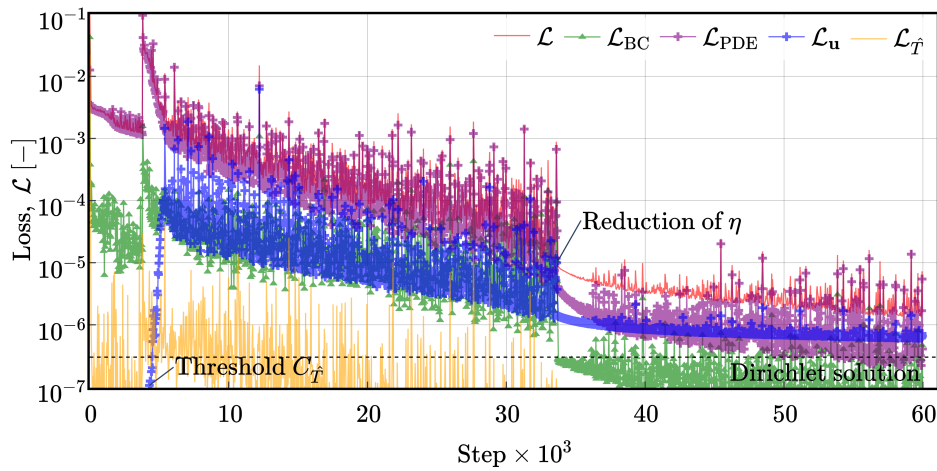


Figure 11: Loss convergence of the 1D model. The plot illustrates the convergence of the total loss and its contributing components: boundary condition, PDE, experimental displacement, and penalty on negative losses. The Dirichlet solution is presented for reference. The fade-in of the displacement loss is visible around 4k epochs. The overall convergence follows a linear trend until $\bar{3}2$ k epochs, where the first learning rate reduction occurs. A final learning rate reduction at the end is barely visible.

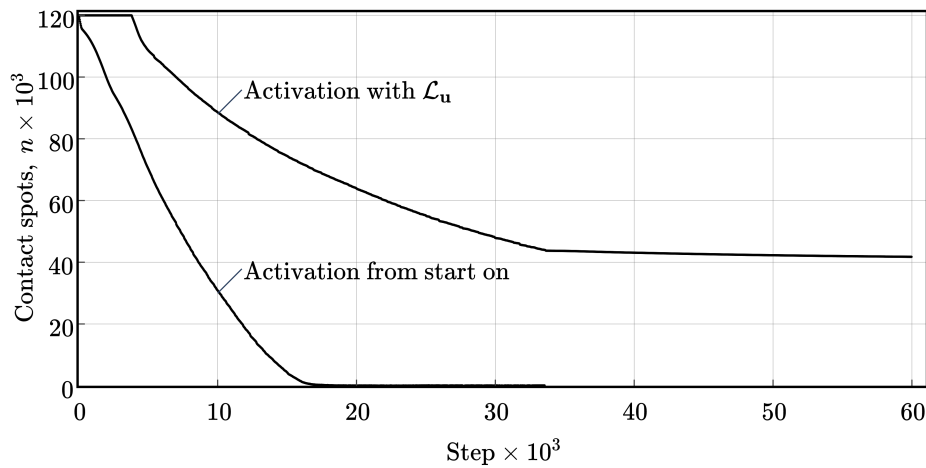


Figure 12: Optimization strategies for the network parameter n . Early activation, from the start on, to the optimizer results in $n \approx 90$, leading to inflated constriction resistance. The value remains about the $n < 1$ threshold for hyperbolic growth. The convergence is not affected once the experimental loss term is added. Delayed addition, alongside experimental data loss, leads to $n \approx 40,000$.

	Train Loss	Test R^2
Forward PINN	17.8×10^{-6}	0.985
Inverse PINN	1.3×10^{-6}	0.974

Table 7: Train loss and accuracy of a forward and inverse PINN.

The model strikes a balance between the optimization criteria. The employed training strategies facilitate efficient convergence. It is essential to note that all separate losses converge, indicating an effective model.

Using Eq. 20 to model the contact heat, the optimization of the number of contact spots, n , is of particular interest because this parameter influences heat generation at the faying surface. Initial experiments, where n was a learnable parameter from the onset of training, resulted in models that aggressively minimized n . This behaviour led to n converging to unreasonable low values around $n \approx 90$, which in turn inflates the constriction resistance part of R_c . Notably, this value is still above the threshold of $n \leq 1$, below which the contact heat would become hyperbolic. Reconsidering the effect of defining contact resistance with n contact spots, it underestimates constriction resistance by \sqrt{n} compared to film resistance. We reason that this is the result of the optimizer prioritizing n , even as the experimental loss \mathcal{L}_u is introduced. To achieve a more physically sound model, n is added to the optimizer once \mathcal{L}_u is introduced. This delay resulted in a convergence to a value of 40,000, effectively more than halving the initial estimate, but still well above 90. The resulting convergence is shown in Fig. 12. We reason that \mathcal{L}_u provides a desirable optimization conflict, which is mediated by n . Still, the initial estimate is off and convergence of n suggests that either the number of initial contact spots n was overestimated or other variables in Eq. 20, e.g., film thickness or film resistance, were assumed too low. Considering that the variance in film resistance spans orders of magnitude (Mousavi et al. 2022; Tang et al. 2013), and the film thickness is only assumed to be of the order of magnitude (S. C. Wang et al. 2001), this seems reasonable. In addition, adhesive remains may influence the contact parameter, as argued by Zhao et al. (2018).

Considering the contact parameter, the question arises whether forward training would save computational resources, reduce optimization complexity, and produce the same result. We compare the inverse approach with a forward PINN that uses Eq. 19 as contact resistance. This comparison can reveal which approach is better for modelling contact heat generation. We evaluate the two methods based on the loss convergence and test accuracy. A forward model is trained using the contact heat generation defined in Eq. 21. This formulation does not require the estimation of n , which can benefit model training. It relies on the constriction resistance and considers a spreading resistance factor. Quantitatively, the resulting loss and accuracy are summarized in Tab. 7. The R^2 has been calculated over 17 time series from $\mathcal{D}^{\text{test}}$. Fig. 13 compares the loss convergence of both model choices. Across several experiments, it is consistently observed that \mathcal{L}_u does not converge as fast or to the same magnitude as the inverse PINN. We deduce that n facilitates convergence by mediating the optimization conflict. However, the forward model is expected to achieve the same result, considering the dynamic displacement. The contact resistance can be calculated backwards from the predicted temperature at the faying surface. Fig. 14 shows the predictions of the inverse and forward models. It is evident that the contact resistances contain different proportions of constriction resistance. The inverse model results in a lower loss. This suggests that the equations were better solved by the inverse model, which effectively underestimated the constriction resistance.

4.2.3 Temperature fields and dynamic displacements

Simulating different current and force levels shows the model’s predictive capabilities. Two extremes are chosen from $\mathcal{D}^{\text{test}}$ to illustrate the range of the temperature fields. The upper extrema is a high $I_{\text{max}} = 47$ with a low $F_{\text{max}} = 5$, and the lower extrema is $I_{\text{max}} = 26$ with $F_{\text{max}} = 8$. Those yield the highest and lowest u and $T(z, t)$ for the EN AW-6014 combination. The temperature fields are shown in Fig. 15 and Fig. 16. The temperature evolution during preheat and hold time is also similar, especially when examining the edges. It is observed that the model handles discontinuity from the welding schedule at $t = 560$ well, cf. Eq. 1. Regarding the displacement field, u is compared to the experimental variance of the data. Recall that one sheet of 30 spots was welded with the same parameters, giving a mean and

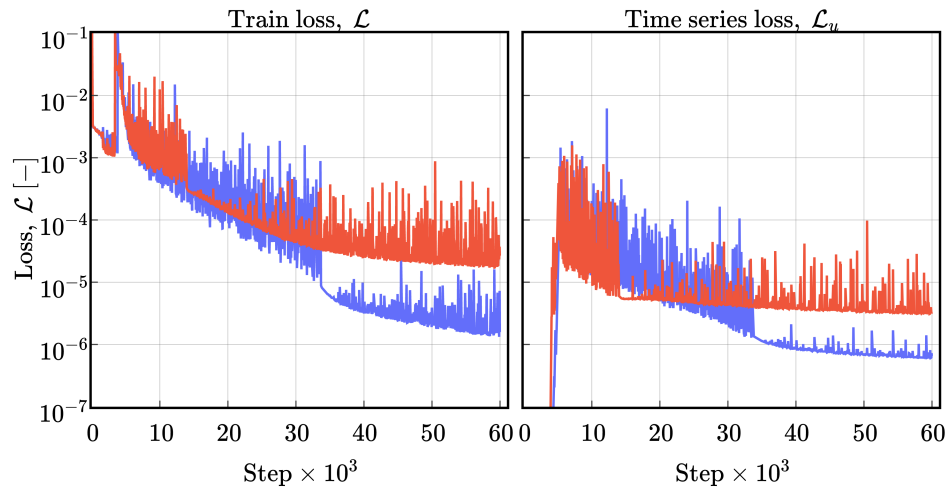


Figure 13: Comparison of a forward and inverse PINN. The blue curve reflects the losses for an inverse and the red curve for a forward PINN. Both models reduce the learning rate once. The inverse model converges to a loss about 8 times lower.

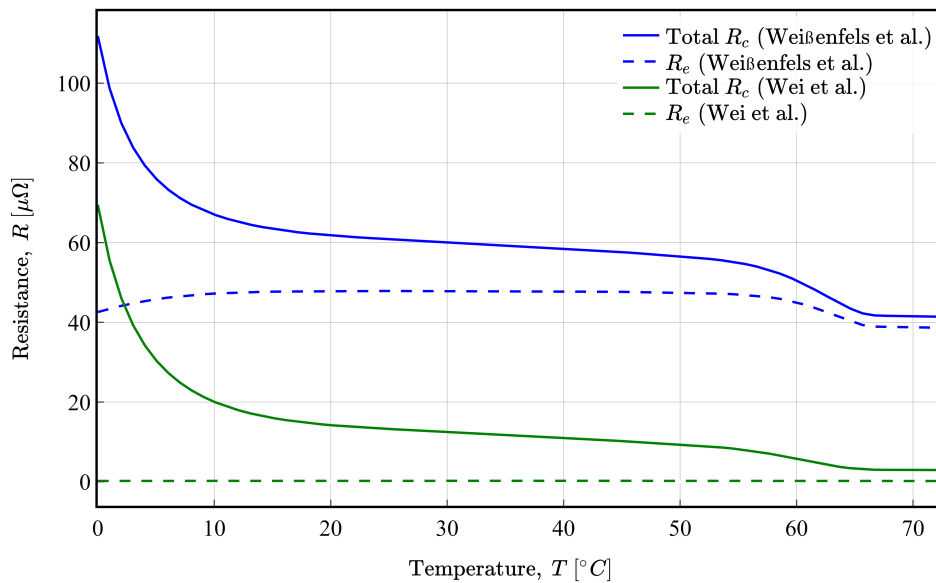


Figure 14: Total contact resistance and its constriction component for the contact equation used in the inverse and forward one-dimensional models. Constriction resistance is calculated from the estimated temperature at each time step. The forward model shows a significant constriction component, while the inverse model estimates a negligible, near-zero constriction resistance.

standard deviation. The mean was used for training the network, while the standard deviation was used to assess its performance. The predicted u lies within the confidence interval with an overall accuracy on $\mathcal{D}^{\text{test}}$ of $R^2 = 0.97$. The prediction was shown to be smoother than the experimental mean.

4.3 Two-dimensional aluminum resistance spot welding

The main limitation of the 2D approach is the substantial increase in computational cost, attributed to a 100-fold increase in collocation points. However, training converged over approximately the same number of epochs as the 1D model. We investigate the training performance of a complete 2D model and the addition of the experimental nugget diameter d_n . The latter is the key benefit of the 2D extension. The same hyperparameters were used for the 2D model, and $\lambda_{d_n} = 10$ was set. The loss convergence is depicted in Fig. 17, showing loss curves for \mathcal{L}_{BC} , \mathcal{L}_{PDE} , \mathcal{L}_u , and $\mathcal{L}_{\hat{T}}$. The time series loss is activated about 2,000 epochs earlier than in Fig. 11 and converges with two learning rate reductions and stops after 1,000 epochs of no improvement. Notably, while the 1D model exhibited a prominent loss spike, the 2D model did not, indicating a different optimization dynamic. The loss preventing negative temperatures essentially vanishes after 25,000 epochs. The magnitude of \mathcal{L} is higher than with the 1D model, but the resulting temperature field does not show unexpected values.

4.3.1 Predicted dynamic displacement

Dynamic displacement curves are of particular interest in RSW for interpreting the nugget development, as they capture and measure the thermal response of the material to the welding process. Although much of the research on dynamic displacement focuses on steel (Dickinson et al. 1990; Gedeon et al. 1986a,b; Gould 1987; Lane et al. 1987; Wei and Ho 1990), the stages of relating to the nugget development identified for steel can be adapted for aluminum. However, aluminum's lower melting point, the absence

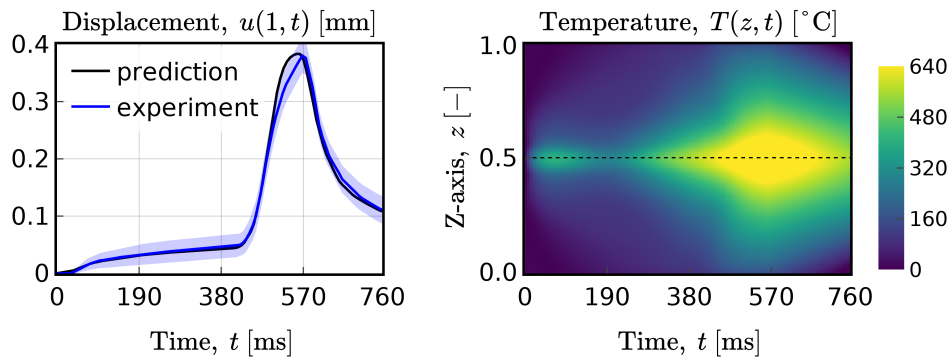


Figure 15: Predicted dynamic displacement and temperature field of the 1D model on unseen test data.

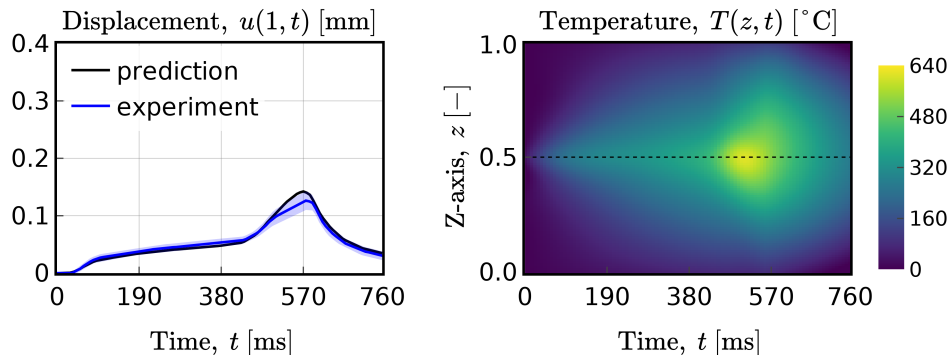


Figure 16: Predicted dynamic displacement and temperature field of the 1D model on unseen test data.

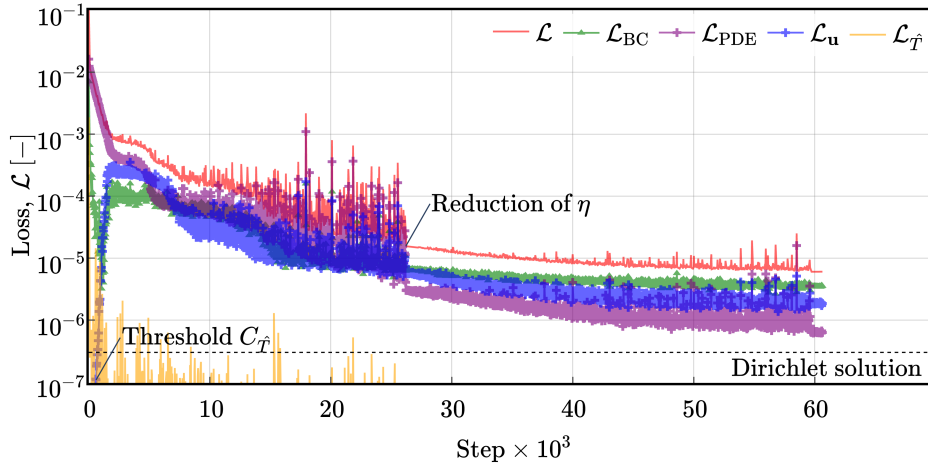


Figure 17: Loss convergence of the 2D model. The plot illustrates the convergence of the total loss and its contributing components: boundary condition, PDE, experimental displacement, and penalty on negative losses. The Dirichlet solution is presented for reference. The loss is elevated compared to the 1D model and convergence is not as straight, cf. 11. The impact of adding the experiential loss is barely visible.

of a zinc coating, or its higher thermal conductivity alter the timing and characteristics of the stages. A comparison of the 1D and 2D models reveals the trade-off of modeling aluminum RSW with a reduced or more complex model. The 1D model predictions on the test data are visualized with the predicted temperature field in Fig. 15 and Fig. 16. The temperature distribution is continuous despite contact heat being a scalar value on the faying surface. This shows that the PDE equations successfully enforce a continuous temperature field. The results from the 2D model are shown in Fig. 19, consisting of 17 test displacement curves from hold-out data. In this figure, the dotted line represents the prediction, while the solid line represents the experimental data. The general trend is well fit, but two observations are visible. First, the initial part is not well fitted, between 0 and 100 ms. Second, the prediction is smoother and mismatches slightly, approaching the curve peak. Some curves exhibit unexplained worse predictions, indicating potential adverse experimental conditions or model accuracy.

Apart from occasional molten material, no nugget development is expected during stage I. This agrees with the 1D model, which predicts the first heating during preheating until $t = 400$. The heat generation is visible for low forces, e.g., Fig. 15. Apart from this effect, u is unaffected during preheating because it is fixed at 12 kA during this time. Stage II is defined by a rapid increase in thermal expansion upon the point where the melting point is reached. This linear increase is visible in u for both models. Stage III marks the slope decrease of u and the beginning of a saturation due to nugget development. This becomes visible once T_{liq} is reached in the temperature field. This means that the end of the linear slope marks the beginning of the nugget development in aluminum RSW. The temperature field indicates the exact timing of nugget formation, as described in stages III and IV. The 1D model predicts the displacement within the confidence interval, but the model systematically overestimates this turning point. The 2D model exhibits a closer fit at this stage. The last part of the welding schedule, the hold time, cools the sheet's surfaces. Our experiments do not exhibit excessive heat generation or spatter, characteristic of stage IV for steel RSW.

4.3.2 Predicted nugget diameter development

While FEM models (Eisazadeh et al. 2010; Hou et al. 2007; Saleem et al. 2012; Tsai et al. 1991) offer valuable insights, they differ from machine learning approaches in that they do not learn from data. In contrast, an advantage of PINNs is their ability to generalize between datapoints, effectively learning from experimental data while adhering to underlying physical relationships. The 2D PINN can predict the complete temperature field $\hat{T}(r, z, t)$ on \mathcal{D}^{test} , including time steps towards the end of the main welding time, $t = 560$, which are essential for the nugget diameter development. The performance is quantified

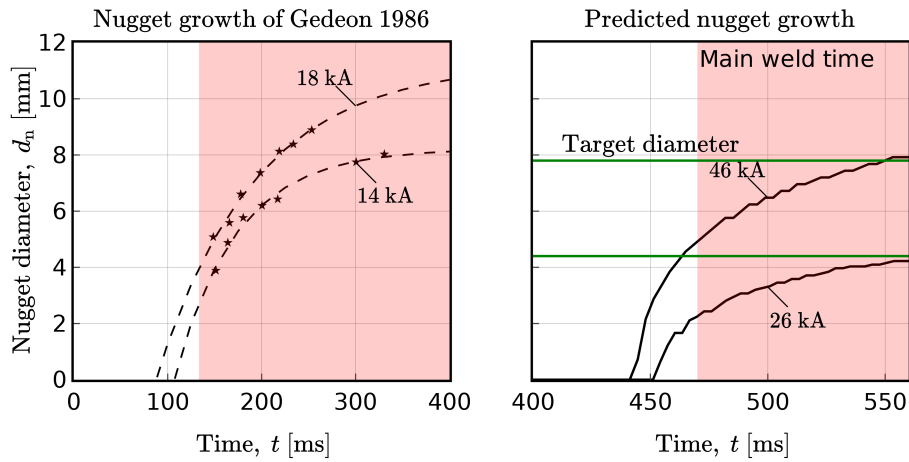


Figure 18: Comparison of the predicted nugget development and data for steel from Gedeon et al. (1986b). The qualitative shape of both is observed to be comparable.

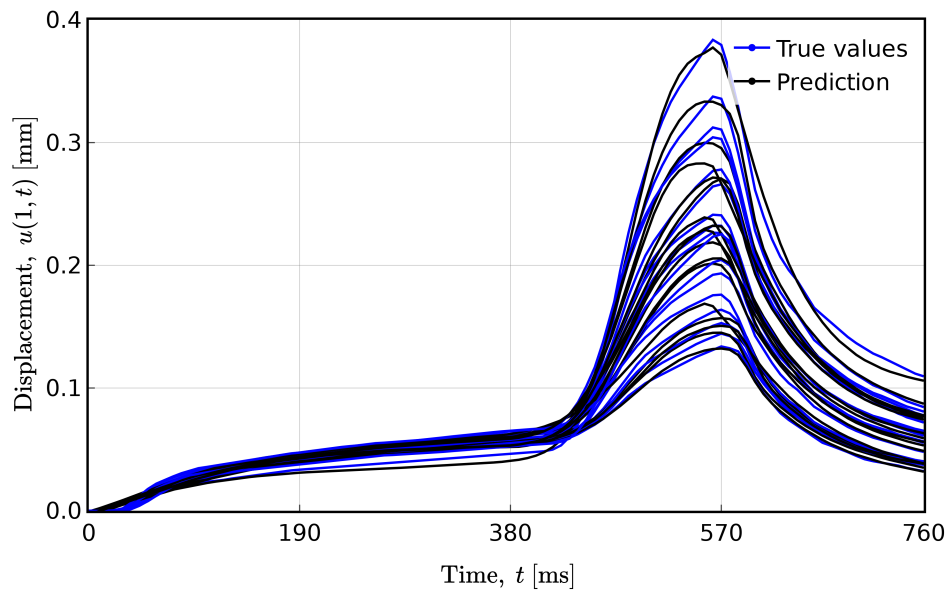


Figure 19: Comparison of experimental dynamic displacement to predictions of the 2D model. Discrepancies are observed during the initial phase, while closer agreement is found during the upslope and main welding phases.

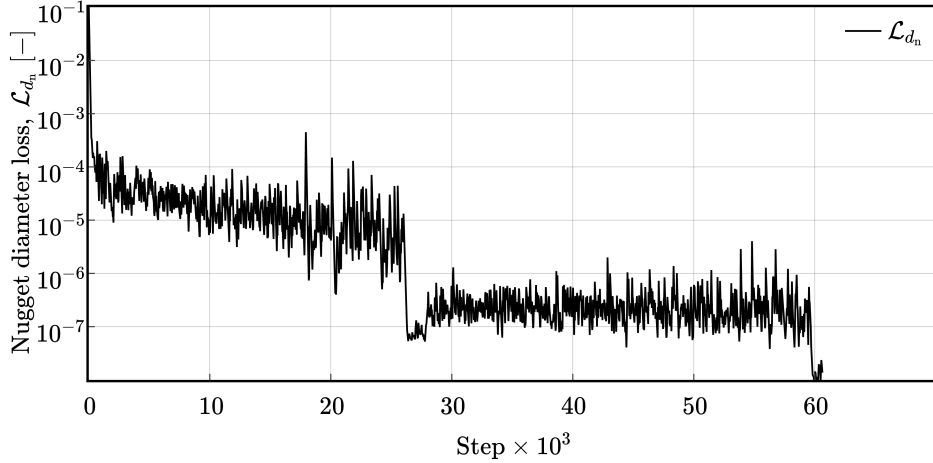


Figure 20: Loss convergence of the nugget diameter loss \mathcal{L}_{d_n} of the 2D model.

by the loss convergence of \mathcal{L}_{d_n} and fit on experimentally measured nugget diameters of $\mathcal{D}^{\text{test}}$. The nugget diameter loss penalizes predicted temperature below the liquidus at $T(r, z, t = 560)$, cf. Eq. 31. This goal loss is tracked during training and depicted in Fig. 20. It convergence to $\mathcal{L}_{d_n} < 10^{-7}$, indicating no optimization problem for the PINN.

Gedeon et al. (1986b) provided experimental data on the nugget growth of galvanized steel. The authors used a similar welding schedule with upslope and main weld time, albeit with lower durations and current levels. Despite the differences in material, the key trend in nugget development is assumed to be comparable. We compare this nugget development by predicting the 2D temperature field and counting mesh points exceeding the liquidus at the faying surface Γ^{ss} for every t . Fig. 18 shows the nugget development of galvanized steel on the left and aluminum on the right. We fit Gedeon’s data with a curve for visual aid. Because of the mesh granularity, some discontinuities are present. This comparison illustrates the material difference. For steel, a four-kiloampere difference over 266 milliseconds resulted in a 2 mm difference in nugget diameter. Meanwhile, aluminum RSW used a 20-kiloampere difference over 90 milliseconds to increase four millimeters. This difference stems from increased thermal conductivity, which is why higher amperages and shorter welding times are typically used. The PINN learns to predict the nugget diameter with acceptable accuracy. The nugget development is visually comparable to steel RSW. The liquidus temperature is reached during the upslope. In the following milliseconds, the nugget develops rapidly, followed by a period of stagnation during the main welding time. This rapid, linear growth corresponds to the dynamic displacement stage II, followed by a stagnation during stage III. With EN AW-6014 we do not observe a stage-IV-expulsion. The nugget prediction is visualized for the full temperature field at selected t for different I_{max} and F_{max} in Figs. 21, 22, and 23. We observe that the temperature field is slightly asymmetric. Fig. 23 estimates remaining liquid material, evident in the time step $t = 760$. In general, the weld nugget forms uniformly and in the form of an ellipse. This was expected but not prescribed in the model.

5 Conclusion

We model aluminum RSW using PINNs, integrating experimental data and governing equations within a single model. The governing equations and boundary conditions were defined to train a PINN to predict the displacement and temperature fields of aluminum RSW. Special attention is directed towards the welding control behavior, as it affects the displacement measurements and contact heat generation, which is important for RSW. Experimental data, including material parameters, dynamic displacement, and nugget diameter, were integrated using training strategies to achieve rapid loss convergence. A 1D model is developed and used to investigate the training strategies. The model captures the dynamic displacement within the experimental variance for various process parameters. The experiments are faster in one dimension as the curse of dimensionality becomes apparent in the second dimension. The 2D model

includes the nugget diameter at the end of the main welding time as an optimization criterion. Therefore, it learns to represent the dynamic displacement and nugget diameter in terms of the displacement and temperature fields. The typical dynamic displacement stages of steel RSW are transferred to the PINN prediction. Regarding the model training, relatively small networks were able to yield fast loss convergence and acceptable accuracy. This efficiency, particularly in the one-dimensional model, makes it valuable for predictive control in industrial applications due to its instant predictive capability. Furthermore, an advantage of the model is its ability to generalize effectively across different datapoints, making it robust for varied experimental conditions. In conclusion, our study demonstrates that integrating experimental data with governing equations through PINNs effectively predicts displacement and temperature fields in aluminum RSW. The resulting reference curves offer valuable insights into the process dynamics. This approach highlights the potential for optimizing welding parameters and the corresponding reference curve using PINNs and guides future research.

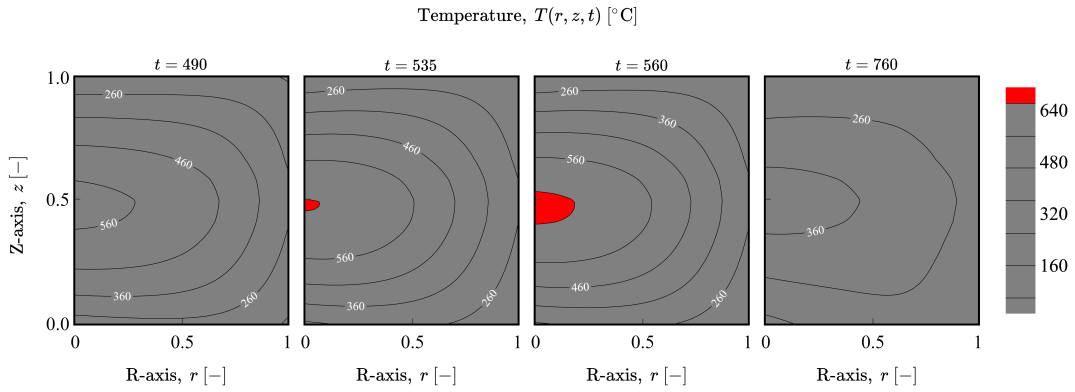


Figure 21: Two-dimensional temperature field $T(r, z, t)$ with $I_{\max} = 26$ and $F_{\max} = 7$.

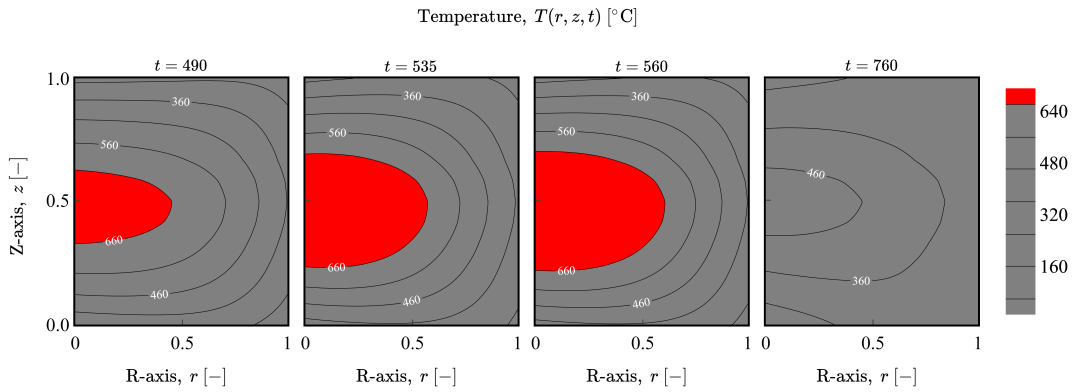


Figure 22: Two-dimensional temperature field $T(r, z, t)$ with $I_{\max} = 32$ and $F_{\max} = 5$.

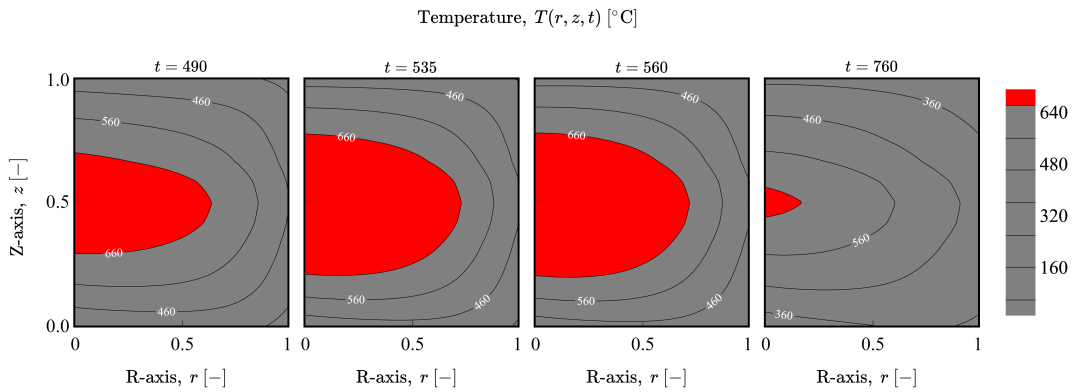


Figure 23: Two-dimensional temperature field $T(r, z, t)$ with $I_{\max} = 43$ and $F_{\max} = 5$.

References

- Adams, R. D. (2021). *Adhesive Bonding: Science, Technology and Applications*. Sawston, UK: Woodhead Publishing. ISBN: 978-0-12-819954-1. DOI: [10.1016/c2019-0-00395-0](https://doi.org/10.1016/c2019-0-00395-0).
- Ao, S.-S. et al. (2009). “Study on quality of resistance spot welded aluminum alloys under various electrode pressures.” In: *Frontiers of Materials Science in China* 3.1, pp. 98–101. ISSN: 1673-7377. DOI: [10.1007/s11706-009-0004-5](https://doi.org/10.1007/s11706-009-0004-5).
- Barnes, T. A. and I. R. Pashby (2000). “Joining techniques for aluminium spaceframes used in automobiles.” In: *Journal of Materials Processing Technology* 99, pp. 62–71. ISSN: 0924-0136. DOI: [10.1016/s0924-0136\(99\)00367-2](https://doi.org/10.1016/s0924-0136(99)00367-2).
- Beltran-Pulido, A., I. Billionis, and D. Aliprantis (2022). “Physics-Informed Neural Networks for Solving Parametric Magnetostatic Problems.” In: *IEEE Transactions on Energy Conversion* 37.4, pp. 2678–2689. ISSN: 0885-8969. DOI: [10.1109/tec.2022.3180295](https://doi.org/10.1109/tec.2022.3180295).
- Bergstra, J., R. Bardenet, et al. (2011). *Algorithms for Hyper-Parameter Optimization*. Conference Paper. URL: <https://proceedings.neurips.cc/paper/2011/file/86e8f7ab32cfd12577bc2619bc635690-Paper.pdf>.
- Bergstra, J. and Y. Bengio (2012). “Random search for hyper-parameter optimization.” In: *Journal of Machine Learning Research* 13, pp. 281–305. ISSN: 1532-4435. URL: <https://www.jmlr.org/papers/volume13/bergstra12a/bergstra12a.pdf>.
- Bergstra, J., D. Yamins, and D. Cox (2013). “Hyperopt: A Python Library for Optimizing the Hyperparameters of Machine Learning Algorithms.” In: *Proceedings of the Python in Science Conference*. Ed. by S. v. d. W. Huff, J. Millman, and Katy. Austin, USA: SciPy, pp. 13–19. DOI: [10.25080/majora-8b375195-003](https://doi.org/10.25080/majora-8b375195-003).
- Boomer, D. R., J. A. Hunter, and D. R. Castle (2003). “A New Approach for Robust High-Productivity Resistance Spot Welding of Aluminium.” In: *SAE Technical Paper Series*. ISSN: 0148-7191. DOI: [10.4271/2003-01-0575](https://doi.org/10.4271/2003-01-0575).
- Bowden, F. P. and D. Tabor (2001). *The Friction and Lubrication of Solids*. Oxford University Press. ISBN: 978-0-19-850777-2. DOI: [10.1093/oso/9780198507772.001.0001](https://doi.org/10.1093/oso/9780198507772.001.0001).
- Bowden, F. P. and J. B. P. Williamson (1958). “Electrical Conduction in Solids. I. Influence of the Passage of Current on the Contact between Solids.” In: *Proceedings of the Royal Society A* 246.1244, pp. 1–12. ISSN: 0080-4630. URL: <http://www.jstor.org/stable/100574>.
- Bowers, R. J., C. D. Sorensen, and T. W. Eagar (1990). “Electrode Geometry Resistance Spot Welding.” In: *Welding Research*, pp. 45–51. ISSN: 0096-7629. URL: https://s3.us-east-1.amazonaws.com/WJ-www.aws.org/supplement/WJ_1990_02_s45.pdf.
- Budynas, R. and K. Nisbett (2020). *Shigley’s Mechanical Engineering Design*. 11th ed. New York, USA: McGraw Hill. ISBN: 978-0-07-339821-1.
- Cai, S. et al. (2022). “Physics-informed neural networks (PINNs) for fluid mechanics: a review.” In: *Acta Mechanica Sinica* 37.12, pp. 1727–1738. ISSN: 0567-7718. DOI: [10.1007/s10409-021-01148-1](https://doi.org/10.1007/s10409-021-01148-1).
- Chen, N. et al. (2019). “Schedule and electrode design for resistance spot weld bonding Al to steels.” In: *Journal of Materials Processing Technology* 265, pp. 158–172. ISSN: 0924-0136. DOI: [10.1016/j.jmatprot.2018.10.011](https://doi.org/10.1016/j.jmatprot.2018.10.011).
- Chen, Y. et al. (2020). “Physics-informed neural networks for inverse problems in nano-optics and metamaterials.” In: *Optics Express* 28.8. ISSN: 1094-4087. DOI: [10.1364/oe.384875](https://doi.org/10.1364/oe.384875).
- Crinon, E. and J. T. Evans (1998). “The effect of surface roughness, oxide film thickness and interfacial sliding on the electrical contact resistance of aluminium.” In: *Materials Science and Engineering: A* 242.1-2, pp. 121–128. ISSN: 0921-5093. DOI: [10.1016/s0921-5093\(97\)00508-x](https://doi.org/10.1016/s0921-5093(97)00508-x).
- Cuomo, S. et al. (2022). “Scientific Machine Learning through Physics-Informed Neural Networks: Where we are and What’s next.” In: *Journal of Scientific Computing* 92.3. ISSN: 1573-7691. DOI: [10.1007/s10915-022-01939-z](https://doi.org/10.1007/s10915-022-01939-z).
- Dickinson, D. W., C.-L. Tsai, and O. Jammal (1990). *Modeling of Resistance Spot Weld Nugget Growth - Applications for the Automotive Industry*. Conference Paper. DOI: [10.4271/900738](https://doi.org/10.4271/900738).
- Dobler, A., H. Koenigsberg, and D. van Winkle (1969). “Developments in Soviet Aerospace Manufacturing Technologies.” In: *SAE Technical Paper Series*. DOI: [10.4271/690701](https://doi.org/10.4271/690701).

- Eagar, T. W. (1990). *The Physics of Welding Processes*. Conference Paper. URL: <https://eagar.mit.edu/publications/Eagar103.pdf>.
- Eckstein, L. et al. (2010). “Analyse sekundärer Gewichtseinsparpotenziale in Kraftfahrzeugen [Analysis of secondary weight saving potentials in vehicles].” In: *ATZ - Automobiltechnische Zeitschrift* 113.1, pp. 68–76. ISSN: 0001-2785. DOI: [10.1365/s35148-011-0015-2](https://doi.org/10.1365/s35148-011-0015-2).
- Eisazadeh, H., M. Hamedi, and A. Halvaei (2010). “New parametric study of nugget size in resistance spot welding process using finite element method.” In: *Materials and Design* 31. DOI: [10.1016/j.matdes.2009.06.042](https://doi.org/10.1016/j.matdes.2009.06.042).
- EU (2019). *No. 2019/631 of the European parliament and of the council of 17 April 2019: setting CO2 emission performance standards for new passenger cars and for new light commercial vehicles, and repealing regulations (EC) No 443/2009 and (EU) No 510/2011*. Legal Rule or Regulation. URL: <https://eur-lex.europa.eu/legal-content/DE/ALL/?uri=CELEX:32019R0631>.
- Farlow, S. J. (1993). *Partial Differential Equations for Scientists and Engineers*. Dover Books on Mathematics. New York, USA: Dover Publications. ISBN: 978-0-486-67620-3.
- Florea, R. S. et al. (2013). “Welding parameters influence on fatigue life and microstructure in resistance spot welding of 6061-T6 aluminum alloy.” In: *Materials and Design* 45, pp. 456–465. ISSN: 02613069. DOI: [10.1016/j.matdes.2012.08.053](https://doi.org/10.1016/j.matdes.2012.08.053).
- Furukawa, K. et al. (2006). “Influence of Electrode Pressure and Welding Conditions on the Maximum Tensile Shear Load.” In: *Quarterly Journal of the Japan Welding Society* 24.1, pp. 10–16. ISSN: 0288-4771. DOI: [10.2207/qjwjs.24.10](https://doi.org/10.2207/qjwjs.24.10).
- Gedeon, S. A. and T. W. Eagar (1986a). “Resistance spot welding of galvanized steel: Part I. Material variations and process modifications.” In: *Metallurgical Transactions B* 17.4, pp. 879–885. ISSN: 1543-1916. DOI: [10.1007/BF02657151](https://doi.org/10.1007/BF02657151).
- (1986b). “Resistance spot welding of galvanized steel: Part II. Mechanisms of spot weld nugget formation.” In: *Metallurgical Transactions B* 17.4, pp. 887–901. ISSN: 1543-1916. DOI: [10.1007/BF02657152](https://doi.org/10.1007/BF02657152).
- Gould, J. E. (1987). “An Examination of Nugget Development during Spot Welding, Using Both Experimental and Analytical Techniques.” In: *Welding Research* 1. ISSN: 0096-7629. URL: https://app.aws.org/wj/supplement/WJ_1987_01_s001.pdf.
- (2012). “Joining Aluminum Sheet in the Automotive Industry - A 30 Year History.” In: *Welding Research* 91, pp. 23–34. ISSN: 0096-7629. URL: https://app.aws.org/wj/supplement/WJ_2012_01_s23.pdf.
- Greenwood, J. A. and J. B. P. Williamson (1958). “Electrical conduction in solids II. Theory of temperature-dependent conductors.” In: *Proceedings of the Royal Society A* 246.1244, pp. 13–31. ISSN: 0080-4630. DOI: [10.1098/rspa.1958.0103](https://doi.org/10.1098/rspa.1958.0103).
- Grohs, P. et al. (2023). *A proof that artificial neural networks overcome the curse of dimensionality in the numerical approximation of Black-Scholes partial differential equations*. Vol. 284. Memoirs of the American Mathematical Society. Providence, USA: American Mathematical Society. ISBN: 978-1-4704-7448-5.
- Grossmann, T. G. et al. (2023). “Can Physics-Informed Neural Networks beat the Finite Element Method?” In: *ArXiv.org*. ISSN: 2331-8422. URL: <https://arxiv.org/abs/2302.04107>.
- He, J., X. Li, and H. Zhu (2023). “An adaptive discrete physics-informed neural network method for solving the Cahn–Hilliard equation.” In: *Engineering Analysis with Boundary Elements* 155, pp. 826–838. ISSN: 0955-7997. DOI: [10.1016/j.enganabound.2023.06.031](https://doi.org/10.1016/j.enganabound.2023.06.031).
- Hennigh, O. et al. (2021). “NVIDIA SimNet: An AI-Accelerated Multi-Physics Simulation Framework.” In: *Computational Science – ICCS 2021*. Vol. 12746. Lecture Notes in Computer Science. Cham, Switzerland: Springer. Chap. 36, pp. 447–461. ISBN: 978-3-030-77976-4. DOI: [10.1007/978-3-030-77977-1_36](https://doi.org/10.1007/978-3-030-77977-1_36).
- Holm, R. (1967). *Electric Contacts*. 4th ed. Springer. ISBN: 978-3-642-05708-3. DOI: [10.1007/978-3-662-06688-1](https://doi.org/10.1007/978-3-662-06688-1).
- Hou, Z. et al. (2007). “Finite element analysis for the mechanical features of resistance spot welding process.” In: *Journal of Materials Processing Technology* 185. DOI: [10.1016/j.jmatprotec.2006.03.143](https://doi.org/10.1016/j.jmatprotec.2006.03.143).

- Hu, J. et al. (2022). “Quality prediction of aluminum alloy resistance spot welding with shunting by introducing spacing factor.” In: *Welding International* 36.12, pp. 716–731. ISSN: 0950-7116. DOI: [10.1080/09507116.2022.2119441](https://doi.org/10.1080/09507116.2022.2119441).
- Hulst, A. P. A. J. (1969). “A thermal model of the spot welding process.” Thesis. DOI: [10.6100/IR155039](https://doi.org/10.6100/IR155039).
- ISO (2009). *DIN EN ISO 5821:2010-04: Resistance welding - Spot welding electrode caps*. Standard. DOI: [10.31030/1560906](https://doi.org/10.31030/1560906).
- (2015). *DIN EN ISO 10447:2015-05: Resistance welding - Testing of welds - Peel and chisel testing of resistance spot and projection welds*. Standard. DOI: [10.31030/2307649](https://doi.org/10.31030/2307649).
- (2016a). *DIN EN ISO 14270:2016-11: Resistance welding - Destructive testing of welds - Specimen dimensions and procedure for mechanized peel testing resistance spot, seam and embossed projection welds*. Standard. DOI: [10.31030/2341919](https://doi.org/10.31030/2341919).
- (2016b). *DIN EN ISO 5182:2016-11: Resistance welding - Materials for electrodes and ancillary equipment*. Standard. DOI: [10.31030/2574960](https://doi.org/10.31030/2574960).
- (2022). *DIN EN ISO 17677-1:2022-02: Resistance welding - Vocabulary - Part 1: Spot, projection and seam welding*. Standard. DOI: [10.31030/3308088](https://doi.org/10.31030/3308088).
- James, P. S. et al. (1997). “The effect of mechanical loading on the contact resistance of coated aluminium.” In: *Materials Science and Engineering: A* 230.1, pp. 194–201. ISSN: 0921-5093. DOI: [10.1016/S0921-5093\(97\)00020-8](https://doi.org/10.1016/S0921-5093(97)00020-8).
- Ji, C. and L. Deng (2010). “Quality control based on electrode displacement and force in resistance spot welding.” In: *Frontiers of Mechanical Engineering in China* 5.4, pp. 412–417. ISSN: 1673-3479. DOI: [10.1007/s11465-010-0114-x](https://doi.org/10.1007/s11465-010-0114-x).
- Ji, C. T. and Y. N. Zhou (2004). “Dynamic Electrode Force and Displacement in Resistance Spot Welding of Aluminum.” In: *Journal of Manufacturing Science and Engineering* 126.3, pp. 605–610. ISSN: 1087-1357. DOI: [10.1115/1.1765140](https://doi.org/10.1115/1.1765140).
- Jung, A. (2022). *Machine Learning*. 1st ed. Machine Learning: Foundations, Methodologies, and Applications. Springer Singapore. ISBN: 978-981-16-8192-9. DOI: [10.1007/978-981-16-8193-6](https://doi.org/10.1007/978-981-16-8193-6).
- Kaars, J., P. Mayr, and K. Koppe (2016a). “Dynamic apparent transition resistance data in spot welding of aluminized 22MnB5.” In: *Data Brief* 8, pp. 1184–9. ISSN: 2352-3409. DOI: [10.1016/j.dib.2016.06.063](https://doi.org/10.1016/j.dib.2016.06.063).
- (2016b). “Generalized dynamic transition resistance in spot welding of aluminized 22MnB5.” In: *Materials and Design* 106, pp. 139–145. ISSN: 0264-1275. DOI: [10.1016/j.matdes.2016.05.097](https://doi.org/10.1016/j.matdes.2016.05.097).
- Kapoor, T. et al. (2024). “Physics-Informed Neural Networks for Solving Forward and Inverse Problems in Complex Beam Systems.” In: *IEEE Transactions on Neural Networks and Learning Systems* 35.5, pp. 5981–5995. ISSN: 2162-237X. DOI: [10.1109/tnnls.2023.3310585](https://doi.org/10.1109/tnnls.2023.3310585).
- Karniadakis, G. E. et al. (2021). “Physics-informed machine learning.” In: *Nature Reviews Physics* 3.6, pp. 422–440. ISSN: 2522-5820. DOI: [10.1038/s42254-021-00314-5](https://doi.org/10.1038/s42254-021-00314-5).
- Kavallaris, N. I. and T. Suzuki (2018). “Resistance Spot Welding.” In: *Non-Local Partial Differential Equations for Engineering and Biology*. 1st ed. Mathematics for Industry. Cham, Switzerland: Springer. Chap. 4, pp. 131–159. ISBN: 978-3-319-67942-6. DOI: [10.1007/978-3-319-67944-0_4](https://doi.org/10.1007/978-3-319-67944-0_4).
- Kim, G.-C. et al. (2018). “Effect of Welding Time on Resistance Spot Weldability of Aluminum 5052 Alloy.” In: *Metals and Materials International* 25.1, pp. 207–218. ISSN: 1598-9623. DOI: [10.1007/s12540-018-0179-3](https://doi.org/10.1007/s12540-018-0179-3).
- Lagaris, I. E., A. Likas, and D. I. Fotiadis (1998). “Artificial neural networks for solving ordinary and partial differential equations.” In: *IEEE Transactions on Neural Networks* 9.5, pp. 987–1000. ISSN: 1045-9227. DOI: [10.1109/72.712178](https://doi.org/10.1109/72.712178).
- Landau, L. D. and E. M. Lifshitz (1986). *Theory of Elasticity*. 3rd ed. Vol. 7. Courses of Theoretical Physics. Butterworth-Heinemann. ISBN: 978-0-08-057069-3. DOI: [10.1016/C2009-0-25521-8](https://doi.org/10.1016/C2009-0-25521-8).
- Lane, C. T. et al. (1987). “Cinematography of Resistance Spot Welding of Galvanized Steel Sheet.” In: *Welding Research*, pp. 260–265. ISSN: 0096-7629. URL: https://app.aws.org/wj/supplement/WJ_1987_09_s260.pdf.
- Langtangen, H. P. and G. K. Pedersen (2016). *Scaling of Differential Equations*. 1st ed. Cham, Switzerland: Springer. ISBN: 978-3-319-32725-9. DOI: [10.1007/978-3-319-32726-6](https://doi.org/10.1007/978-3-319-32726-6).

- Leitner, M. et al. (2017). “Thermophysical Properties of Liquid Aluminum.” In: *Metallurgical and Materials Transactions A* 48.6, pp. 3036–3045. ISSN: 1073-5623. DOI: [10.1007/s11661-017-4053-6](https://doi.org/10.1007/s11661-017-4053-6).
- Li, Y. B., Z. Q. Lin, S. J. Hu, et al. (2007). “Numerical analysis of magnetic fluid dynamics behaviors during resistance spot welding.” In: *Journal of Applied Physics* 101.5. ISSN: 0021-8979. DOI: [10.1063/1.2472279](https://doi.org/10.1063/1.2472279).
- Li, Y. B., Z. Q. Lin, X. M. Lai, et al. (2009). “Electromagnetic phenomena in resistance spot welding and its effects on weld nugget formation.” In: *Progress In Electromagnetics Research Symposium Proceedings*. Moscow, Russia: The Electromagnetics Academy, pp. 744–748. ISBN: 978-1-934142-10-3.
- Lienert, T. et al. (2011). *ASM Handbook: Welding Fundamentals and Processes*. Vol. 6A. ASM International. ISBN: 978-1-62708-174-0. DOI: [10.31399/asm.hb.v06a.9781627081740](https://doi.org/10.31399/asm.hb.v06a.9781627081740).
- Lienhard, J. H. and J. H. Lienhard (2020). *A Heat Transfer Textbook*. 5th ed. Mineola, USA: Dover Publications. ISBN: 978-0-486-83735-2. URL: <http://ahtt.mit.edu>.
- Lifeng, Y., Z. Zuohua, and C. Haipeng (2004). “Finite element analysis of thermal field and flow field in spot welding for aluminum alloys.” In: *Transactions of the China welding institution* 6, pp. 4–6.
- Lu, L. (2020). “Theory, Algorithms, and Software for Physics-Informed Deep Learning.” Thesis. DOI: [10.26300/mpz0-gr82](https://doi.org/10.26300/mpz0-gr82).
- Luo, Z. et al. (2015). “Application of Pre-heating to Improve the Consistency and Quality in AA5052 Resistance Spot Welding.” In: *Journal of Materials Engineering and Performance* 24.10, pp. 3881–3891. ISSN: 1059-9495. DOI: [10.1007/s11665-015-1704-x](https://doi.org/10.1007/s11665-015-1704-x).
- McKay, M. D., R. J. Beckman, and W. J. Conover (1979). “A Comparison of Three Methods for Selecting Values of Input Variables in the Analysis of Output from a Computer Code.” In: *Technometrics* 21.2. ISSN: 0040-1706. DOI: [10.2307/1268522](https://doi.org/10.2307/1268522).
- Mills, K. C. (2002). *Recommended values of thermophysical properties for selected commercial alloys*. Recommended Values of Thermophysical Properties for Selected Commercial Alloys. Woodhead Publishing. ISBN: 978-1-85573-569-9. DOI: [10.1533/9781845690144](https://doi.org/10.1533/9781845690144).
- Moseley, B., A. Markham, and T. Nissen-Meyer (2020). “Solving the wave equation with physics-informed deep learning.” In: *ArXiv.org*. ISSN: 2331-8422. URL: <https://arxiv.org/abs/2006.11894>.
- Mousavi, S. R. et al. (2022). “A review of electrical and thermal conductivities of epoxy resin systems reinforced with carbon nanotubes and graphene-based nanoparticles.” In: *Polymer Testing* 112. ISSN: 0142-9418. DOI: [10.1016/j.polymertesting.2022.107645](https://doi.org/10.1016/j.polymertesting.2022.107645).
- Piott, M. et al. (2019). “Electrical Contact Resistance Model for Aluminum Resistance Spot Welding.” In: *Mathematical Modelling of Weld Phenomena 12*. Ed. by C. Sommitsch, N. Enzinger, and P. Mayr. Graz, Austria: Verlag der Technischen Universität Graz. DOI: [10.3217/978-3-85125-615-4-36](https://doi.org/10.3217/978-3-85125-615-4-36).
- (2020). “A study of the heat transfer mechanism in resistance spot welding of aluminum alloys AA5182 and AA6014.” In: *The International Journal of Advanced Manufacturing Technology* 111.1-2, pp. 263–271. ISSN: 0268-3768. DOI: [10.1007/s00170-020-05650-x](https://doi.org/10.1007/s00170-020-05650-x).
- Poggio, T. et al. (2017). “Why and when can deep-but not shallow-networks avoid the curse of dimensionality: A review.” In: *International Journal of Automation and Computing* 14.5, pp. 503–519. ISSN: 1476-8186. DOI: [10.1007/s11633-017-1054-2](https://doi.org/10.1007/s11633-017-1054-2).
- Prabitz, K. et al. (2021). “Validated Multi-Physical Finite Element Modelling of the Spot Welding Process of the Advanced High Strength Steel DP1200HD.” In: *Materials* 14.18. ISSN: 1996-1944. DOI: [10.3390/ma14185411](https://doi.org/10.3390/ma14185411).
- Prechelt, L. (2012). “Early Stopping — But When?” In: *Neural Networks: Tricks of the Trade*. Lecture Notes in Computer Science. Berlin, Germany: Springer. Chap. Chapter 5, pp. 53–67. ISBN: 978-3-642-35288-1. DOI: [10.1007/978-3-642-35289-8_5](https://doi.org/10.1007/978-3-642-35289-8_5).
- Raissi, M., P. Perdikaris, and G. E. Karniadakis (2017a). “Physics Informed Deep Learning (Part I): Data-driven Solutions of Nonlinear Partial Differential Equations.” In: *ArXiv.org*. ISSN: 2331-8422. URL: <https://arxiv.org/abs/1711.10561>.
- (2017b). “Physics Informed Deep Learning (Part II): Data-driven Discovery of Nonlinear Partial Differential Equations.” In: *ArXiv.org*. ISSN: 2331-8422. URL: <https://arxiv.org/abs/1711.10566>.
- Raissi, M., A. Yazdani, and G. E. Karniadakis (2020). “Hidden fluid mechanics: Learning velocity and pressure fields from flow visualizations.” In: *Science* 367.6481, pp. 1026–1030. ISSN: 0036-8075. DOI: [10.1126/science.aaw4741](https://doi.org/10.1126/science.aaw4741).

- Roth, R., J. Clark, and A. Kelkar (2001). “Automobile bodies: Can aluminum be an economical alternative to steel?” In: *Journal of The Minerals, Metals and Materials Society* 53.8, pp. 28–32. ISSN: 1047-4838. DOI: [10.1007/s11837-001-0131-7](https://doi.org/10.1007/s11837-001-0131-7).
- Saleem, J. et al. (2012). “Nugget Formation during Resistance Spot Welding using Finite Element Model.” In: *World Academy of Science, Engineering and Technology* 67.
- Seo, J. (2024). “Solving real-world optimization tasks using physics-informed neural computing.” In: *Scientific Reports* 14.1. ISSN: 2045-2322. DOI: [10.1038/s41598-023-49977-3](https://doi.org/10.1038/s41598-023-49977-3).
- Sitzmann, V. et al. (2020). “Implicit Neural Representations with Periodic Activation Functions.” In: *34th Conference on Neural Information Processing Systems*. Curran Associates Inc. ISBN: 978-1-71382-954-6. URL: <https://dl.acm.org/doi/10.5555/3495724.3496350>.
- Sun, L. et al. (2020). “Surrogate modeling for fluid flows based on physics-constrained deep learning without simulation data.” In: *Computer Methods in Applied Mechanics and Engineering* 361. ISSN: 0045-7825. DOI: [10.1016/j.cma.2019.112732](https://doi.org/10.1016/j.cma.2019.112732).
- Tang, L.-C. et al. (2013). “Fracture toughness and electrical conductivity of epoxy composites filled with carbon nanotubes and spherical particles.” In: *Composites Part A: Applied Science and Manufacturing* 45, pp. 95–101. ISSN: 1359-835X. DOI: [10.1016/j.compositesa.2012.09.012](https://doi.org/10.1016/j.compositesa.2012.09.012).
- Touloukian, Y. S. and E. H. Buyco (1971). *Specific Heat - Metallic Elements and Alloys. (Reannouncement). Data book*. Vol. 4. Thermophysical Properties of Matter - The TPRC data series. West Lafayette, USA: Springer Science+Business Media. URL: <https://www.osti.gov/biblio/5439707>.
- Touloukian, Y. S., R. K. Kirby, et al. (1975). *Thermal Expansion - Metallic Elements and Alloys. Data book*. Vol. 12. Thermophysical Properties of Matter - The TPRC data series. West Lafayette, USA: Springer Science+Business Media. URL: <https://www.osti.gov/biblio/5439716>.
- Touloukian, Y. S., R. W. Powell, et al. (1970). *Thermal Conductivity - Metallic Elements and Alloys. Data book*. Vol. 1. Thermophysical Properties of Matter - The TPRC data series. West Lafayette, USA: Springer Science+Business Media. URL: <https://www.osti.gov/biblio/5447756>.
- Tsai, C.-L., W. L. Dai, and D. W. Dickinson (1991). “Analysis and Development of A Real-Time Control Methodology in Resistance Spot Welding.” In: *SAE Transactions* 100, pp. 158–176. ISSN: 0096-736X. URL: <http://www.jstor.org/stable/44581115>.
- Wang, J. et al. (2015). “Analysis of Al-steel resistance spot welding process by developing a fully coupled multi-physics simulation model.” In: *International Journal of Heat and Mass Transfer* 89, pp. 1061–1072. ISSN: 0017-9310. DOI: [10.1016/j.ijheatmasstransfer.2015.05.086](https://doi.org/10.1016/j.ijheatmasstransfer.2015.05.086).
- Wang, L. et al. (2023). “Physics-informed neural networks for transcranial ultrasound wave propagation.” In: *Ultrasonics* 132. ISSN: 0041-624X. DOI: [10.1016/j.ultras.2023.107026](https://doi.org/10.1016/j.ultras.2023.107026).
- Wang, S. C. and P. S. Wei (2001). “Modeling Dynamic Electrical Resistance During Resistance Spot Welding.” In: *Journal of Heat Transfer* 123.3, pp. 576–585. ISSN: 0022-1481. DOI: [10.1115/1.1370502](https://doi.org/10.1115/1.1370502).
- Wang, S., S. Sankaran, et al. (2023). “An Expert’s Guide to Training Physics-informed Neural Networks.” In: *ArXiv.org*. ISSN: 2331-8422. URL: <https://arxiv.org/abs/2308.08468>.
- Wang, S., Y. Teng, and P. Perdikaris (2021). “Understanding and Mitigating Gradient Flow Pathologies in Physics-Informed Neural Networks.” In: *SIAM Journal on Scientific Computing* 43.5, A3055–A3081. ISSN: 1064-8275. DOI: [10.1137/20m1318043](https://doi.org/10.1137/20m1318043).
- Wang, S., X. Yu, and P. Perdikaris (2022). “When and why PINNs fail to train: A neural tangent kernel perspective.” In: *Journal of Computational Physics* 449. ISSN: 0021-9991. DOI: [10.1016/j.jcp.2021.110768](https://doi.org/10.1016/j.jcp.2021.110768).
- Wei, P. S. and P. Y. Ho (1990). “Axisymmetric Nugget Growth During Resistance Spot Welding.” In: *Journal of Heat Transfer* 112.2, pp. 309–316. ISSN: 0022-1481. DOI: [10.1115/1.2910377](https://doi.org/10.1115/1.2910377).
- Wei, P. S., S. C. Wang, and M. S. Lin (1996). “Transport Phenomena During Resistance Spot Welding.” In: *Journal of Heat Transfer* 118.3, pp. 762–773. ISSN: 0022-1481. DOI: [10.1115/1.2822697](https://doi.org/10.1115/1.2822697).
- Wei, P. S. and T. H. Wu (2012). “Electrical contact resistance effect on resistance spot welding.” In: *International Journal of Heat and Mass Transfer* 55.11-12, pp. 3316–3324. ISSN: 0017-9310. DOI: [10.1016/j.ijheatmasstransfer.2012.01.040](https://doi.org/10.1016/j.ijheatmasstransfer.2012.01.040).

-
- Wei, P. S. and T. H. Wu (2014). “Effects of electrode contact condition on electrical dynamic resistance during resistance spot welding.” In: *Science and Technology of Welding and Joining* 19.2, pp. 173–180. ISSN: 1362-1718. DOI: [10.1179/1362171813y.0000000177](https://doi.org/10.1179/1362171813y.0000000177).
- Weißenfels, C. and P. Wriggers (2009). “Numerical modeling of electrical contacts.” In: *Computational Mechanics* 46.2, pp. 301–314. ISSN: 0178-7675. DOI: [10.1007/s00466-009-0454-8](https://doi.org/10.1007/s00466-009-0454-8).
- Wessels, H., C. Weißenfels, and P. Wriggers (2020). “The neural particle method – An updated Lagrangian physics informed neural network for computational fluid dynamics.” In: *Computer Methods in Applied Mechanics and Engineering* 368. ISSN: 0045-7825. DOI: [10.1016/j.cma.2020.113127](https://doi.org/10.1016/j.cma.2020.113127).
- Woo, K. L. and T. R. Thomas (1980). “Contact of rough surfaces: A review of experimental work.” In: *Wear* 58.2, pp. 331–340. ISSN: 0043-1648. DOI: [10.1016/0043-1648\(80\)90162-3](https://doi.org/10.1016/0043-1648(80)90162-3).
- Zhang, E. et al. (2022). “Analyses of internal structures and defects in materials using physics-informed neural networks.” In: *Science Advances* 8.7. ISSN: 2375-2548. DOI: [10.1126/sciadv.abk0644](https://doi.org/10.1126/sciadv.abk0644).
- Zhao, Y., Y. Zhang, and X. M. Lai (2018). “Effect of Epoxy Adhesive on Nugget Formation in Resistance Welding of SAE1004/DP600/DP780 Steel Sheets.” In: *Materials* 11.10, p. 1828. ISSN: 1996-1944. DOI: [10.3390/ma11101828](https://doi.org/10.3390/ma11101828).